UNIVERSIDAD NACIONAL AUTÓNOMA DE MÉXICO

POSGRADO EN CIENCIAS FÍSICAS

INSTITUTO DE CIENCIAS NUCLEARES

MEASUREMENT OF ϕ (1020) RESONANCE PRODUCTION IN p-Pb COLLISIONS AT $\sqrt{s_{NN}}$ = 5.02 TeV WITH THE ALICE EXPERIMENT

TESIS

QUE PARA OPTAR POR EL GRADO DE:

MAESTRO EN CIENCIAS FÍSICAS (FÍSICA)

PRESENTA:

EDGAR PÉREZ LEZAMA

TUTOR PRINCIPAL:

DR. GUY PAIC

INSTITUTO DE CIENCIAS NUCLEARES

MIEMBROS DEL COMITÉ TUTOR:

DR. ELEAZAR CUAUTLE FLORES

INSTITUTO DE CIENCIAS NUCLEARES

DR. VARLEN GRABSKI

INSTITUTO DE FÍSICA

MÉXICO, D. F. Septiembre 2014

Dedico esta tesis a mis amados padres ...

Agradecimientos

El mayor y principal agradecimiento es a mis padres, Ángeles Lezama y Jorge Pérez, por su apoyo incondicional a lo largo de esta trayectoria y por su dedicación para darme una formación académica. Agradezco mis tíos y en especial Martha Pérez, Ramón López y Eduardo Pérez, quienes fueron parte importante de este nuevo logro profesional y de alguna u otra manera estuvieron apoyándome y alentándome para poder obtener este importante logro.

Al Dr. Guy Paic, mi asesor, le estaré siempre agradecido por dedicar tiempo en mi formación como cientifico y tambien por ayudarme a que este trabajo trascendiera internacionalmente. Gracias por todas las discusiones en el grupo del ICN.

Le doy las gracias a mis tutores y sinodales Eleazar Cuautle, Varlen Grabski, Lukas Nellen, Ernesto Belmont, Andrés Sandoval y Gerardo Herrera por dedicar parte de su tiempo en leer mi tesis y aportarme valiosas sugerencias y opiniones que finalmente ayudaron a mejorar este trabajo.

Agradezco a mis amigos de la carrera: Tonatiuh Jiménez, Ricardo Román, Iván Toledano, Miguel López y Martín Zumaya, por apoyarme y alentarme en el sinuoso camino de la ciencia. Espero que nuestra amistad y colaboración se mantenga por mucho tiempo. Especial agradecimiento a Antonio Ortiz por motivarme en la fisica de altas energias y darme consejos muy valiosos para mejorar mi trabajo y mi entendimiento de la física. Gracias a Enrique Patiño por proporcionarme material y equipo del laboratorio de detectores.

My completion of this thesis could not have been accomplished without the support and help of the Resonance Group and specially from Ajay Kumar Dash, Francesca Bellini, Anders Knospe, Viktor Riabov, Mikhail Malaev and Christina Markert. The weekly discussions helped me to improve this work. Thanks to the ALICE collaboration for all your comments and suggestions.

La conclusion de este trabajo no hubiera sido posible sin los apoyos economicos que financiaron mis estudios de maestria. Gracias a la beca CONACyT, los apoyos PAEP, el convenio CERN-UNAM, al ICN y especialmente a Alejandro Ayala y a Miguel Alcubierre por apoyarme y darme la oportunidad de realizar estancias en CERN, donde adquirí mucha experiencia y conocimiento por parte de los expertos en el area.

Contents

Resumen

0.1 Introducción

La física de altas energías ha establecido y validado durante las últimas decadas una detallada, pero incompleta, teoría de partículas elementales y sus interacciones fundamentales llamada *Modelo Estándar*. Este modelo ha explicado exitosamente una serie de resultados experimentales y ha predicho de manera precisa una amplia variedad de fenómenos.

De acuerdo con la teoría del Modelo Estándar toda la materia está constituida de tres tipos de partículas elementales: leptones, quarks y las partículas mediadoras. En total son doce partículas, seis quarks: up, down, strange, charm, bottom y top, y seis leptones: electrón, neutrino del electrón, muón, neutrino del muón, tauón y neutrino del tau. Los quarks y los leptones se clasifican dentro de la categoria de los fermiones, por tener espín semientero.

El Modelo Estándar considera tres tipos de interacciones fundamentales y estas se producen a través del intercambio de bosones (espín entero) o partículas mediadoras. El fotón(γ) es la partícula mediadora de la interacción electromagnética, los bosones vectoriales($W^{\pm}$ y Z^0) son responsables de la interacción débil, y los ocho gluones(g) son los mediadores de la interacción fuerte.

El Modelo Estándard tiene, sin embargo, limitaciones que requieren extensiones para mantener la teoria consistente. El aspecto más importante es las masas de los bosones de norma electro-débiles ($W^{\pm}$ y Z^0) que se predicen que deberían ser nulas en la teoría. Lo cual es claramente inconsistente con la teoría. Esta discrepancia puede ser resuelta agregando un bosón de norma adicional, añadido a la teoría, el bosón de Higgs. El mecanismo de Higgs genera las masas para los $W^{\pm}$ y Z^0 mientras que los fotones permanecen sin masa. Resultados recientes del LHC han confirmado la existencia de una partícula desconocida con una masa entre 125 y 127 GeV/c^2. En marzo del 2013 se probó que la partícula desconocida se comportaba, interactuaba y decaia en muchas de las formas predichas por el

Modelo Estárdar, y fue tentativamente confirmado de tener paridad positiva y espín cero, dos atributos fundamentales del bosón de Higgs.

0.1.1 Resonancias

El estudio de la producción de resonancias mesónicas $\phi(1020)$ y $K^*(892)$ tiene su particular importancia. Estas partículas tienen masas muy cercanas pero sus tiempos de vida difieren por un factor alrededor de 10, siendo: $\tau_\phi = 46$ fm/c and $\tau_{K^{*0}} = 4.0$ fm/c, y su contenido de extrañeza o número de quarks extraños difieren por una unidad. Se espera que el K^{*0} sea mas sensitivo a efectos de re-dispersión en el medio hadrónico, debido a su corto tiempo de vida. Por otro lado, el mesón ϕ puede escapar del medio hadrónico casi sin re-dispersión, por esto, esta resonancia es un buen candidato para investigar restauración parcial de simetría quiral en el tiempo de formación. Además, el ϕ es de gran ayuda para probar la producción extrañeza, siendo el mesón vectorial más ligero compuesto de quarks del mar ($s\overline{s}$).

0.2 Experimento ALICE

EL LHC[1] (Gran Colisionador de Hadrones) comenzó como una idea a mediados de la década de los 80's. Anteriormente el CERN[2] (Organización Europea para la Investigación Nuclear) contaba con el colisionador LEP[3] (Gran Colisionador Electrón-Positrón), que funcion de 1989 hasta el ao 2000. EL LHC se encuentra ubicado en la frontera Franco-Suiza cerca de Ginebra, y enterrado a una profundidad entre 50m y 175m. El LHC es un sincrotrón que acelera paquetes de partículas en anillos separados y en sentidos contrarios, cada paquete viaja muchas veces alrededor del anillo del acelerador hasta que se alcanza suficiente energía para colisionarlas. La energía máxima de aceleración para protones es de 7 TeV y 2.76 TeV por nucleón en iones de plomo. Con esto, se alcanzan energías en el centro de masa de la colisión de $\sqrt{s}$=14 TeV para protón-protón, $\sqrt{s_{NN}}$=5.02 TeV p-Pb y $\sqrt{s_{NN}}$=5.5 TeV en iones de plomo.

Para mantener los haces enfocados y acelerados hasta el momento de la colisión, el acelerador tiene que guiarlos a lo largo del anillo. Para lograr esto, el LHC cuenta con 1232 dipolos de 14.3 m de longitud, que desvían la trayectoria de las partículas. Los dipolos contienen magnetos superconductores que operan a una temperatura de $1.9°K$, lo cual está $0.8°K$ por

[1] Large Hadron Collider
[2] Centree Européenne pour la Recherche Nucléaire.
[3] Large Electro-Positron Collider

debajo de la temperatura de fondo del universo, esta temperatura se logra utilizando helio en estado superfluido. Para enfocar los haces, se tienen 392 cuadrupolos con una longitud entre 5 y 7 metros.

El experimento ALICE (A Large Ion Collider Experiment) tiene 16m de alto, 26 m de largo y pesa aproximadamente 10,000 toneladas, ALICE es el cuarto de los grandes experimentos del CERN, que explorará la nueva física que surja a partir de colisionar nucleos de iones contra nucleos de iones (Pb-Pb) a energías del LHC, permitiendo el estudio de la física del equilibrio y del no equilibrio de materia interaccionando fuertemente en densidades del orden de $\varepsilon \simeq 1 - 1000\text{GeVfm}^{-3}$.

El objetivo de ALICE es estudiar a la materia que se encuentra bajo condiciones de densidad extrema, formando así un nuevo estado de la materia llamado *plasma de quarks y gluones (QGP[1])*. La materia en este estado se encuentra 100,000 veces más caliente que el núcleo del sol y bajo estas condiciones los protones y neutrones se funden, liberando así los quarks y gluones que conforman a estos hadrones. Debido a que ningún quark ni gluón han sido observados de forma aislada, siempre están unidos dentro de los hadrones, el estudio de las propiedades del QGP será clave para la Cromodinámica Cuántica en un mejor entendimiento del fenómeno de *Confinamiento*[2]. El experimento ALICE es un experimento de propósito general cuyos detectores miden e identifican hadrones, leptones y fotones. Esto se ha logrado analizando un amplio rango de momento (desde $\sim$ 0.1GeV hasta $\sim$ 100GeV) utilizando las técnicas de identificación conocidas: pérdida de energía por ionización dE/dx, tiempo de vuelo, radiación Cherenkov y de transición, calorimetría electromagnética y filtros de muones.

0.2.1 Detectores TPC y TOF

TPC

El detector TPC o Cámara de Proyección Temporal, es el principal detector de trazas que está optimizado para, junto con los otros detectores cilíndricos, medir el momento de partículas cargadas, identificar el tipo de partícula y determinar la posición del vértice. El volúmen de este detector, de forma cilíndrica, está delimitado por un radio interno de 84.8 cm y el radio externo de 246.6 cm, cubre una longitud de 500 cm en la dirección del haz (eje z).

El espacio fase cubierto por la TPC en psudorapidez es $\mid \eta \mid$<0.9 para trazas de partículas

[1]Por sus siglas en inglés Quark-Gluon Plasma.
[2]Los quarks y gluones están confinados dentro de los hadrones.

radiales. Por ser de forma cilíndrica, cubre completamente el ángulo azimutal (con excepción de las zonas muertas), así mismo cubre un amplio rango de p_t con buena resolución, desde 0.1 GeV hasta 100 GeV.

El detector consiste principalmente de dos partes: la jaula del campo y el electrodo central. La primera es llenada con 90 m^3 de una mezcla de gases: $Ne/CO_2/N_2$ (90/10/5), las partículas cargadas que atraviesen este gas excitarán e ionizarán los átomos de la mezcla a lo largo de la trayectoria de la partícula. Como consecuencia de esta ionización, las partículas irán progresivamente perdiendo energía por unidad de longitud de la traza (dE/dx), la pérdida de energía es específica y característica según el tipo de partícula que está atravesando la TPC. Los electrones son transportados, a lo largo de 2.5 m hacia las tapas del cilindro de la TPC a causa de un fuerte campo eléctrico generado entre las tapas exteriores y el electrodo central, debido a que este último está a un alto voltaje negativo y las tapas externas a un alto voltaje positivo.

Las tapas circulares de la TPC son las que detectan los electrones arrastrados desde el punto de ionización, cada tapa está conformada de 18 sectores trapezoidales que son MWPC[1] (Cámara Proporcional de Multialambres). El MWPC consiste en una serie de rejillas de cátodos y ánodos a diferentes voltajes. Un ánodo está a un voltaje positivo de 1500V, lo cual conlleva a una amplificación de los electrones arrastrados, pues estos incrementan su energía debido al potencial, causando mayores ionizaciones y comenzando así una avalancha de electrones. La señal que reciben los *pads*[2] son proporcionales al número de electrones y a la energía perdida de las partículas cargadas ionizantes. Pero esta proporcionalidad se estropearía si los fotones, que son generados en la avalancha, viajaran más distancia que el tamaño de la avalancha, creando así otras nuevas avalanchas que no serían provenientes directamente de los electrones arrastrados, este efecto es minimizado por los gases CO_2 y N_2 que tienen un alto coeficiente de fotoabsorción sobre un amplio rango de longitud de onda.

TOF

El detector de Tiempo de Vuelo (TOF), cubre una región central de pseudorapidez de $|\eta|<0.9$, es capaz de identificar partículas de un rango de momento intermedio de 0.4 a 2.5GeV para piones y kaones o hasta 4GeV para protones, con una separación mayor a 3σ entre π/K y K/p, esto último se utilizó en esta tesis como método de identificación de partículas en el TOF y se explicará en el siguiente capítulo.

[1] Por sus siglas en inglés Multi-Wire Proportional Chamber.
[2] Elementos sensibles a la detección de electrones.

El detector cubre una superficie cilíndrica con una aceptancia en el ángulo polar entre 45° y 135°. El radio interno del cascarón cilíndrico es de 370 cm y el radio externo de 399 cm, con una longitud de 741 cm en la dirección z. La estructura modular del TOF cuenta con 18 sectores distribuidos en el ángulo azimutal (ϕ) y este arreglo se repite en cinco módulos en la dirección z.

Los módulos contienen un total de 1638 elementos detectores, llamados MRPC (*Multi-gap Resistive Plate Chamber*), y cubren un área de 160 m^2. La principal característica de estas cámaras es su fuerte campo eléctrico y uniforme en todo el volúmen gaseoso[1] del detector, ocasionando que las ionizaciones, debidas a las partículas cargadas producidas en la colisión, generen inmediatamente avalanchas de partículas que producirán señales. Debido a que no existe tiempo de arrastre asociado a los electrones en movimiento, a diferencia de la TPC donde si existe, el tiempo de vuelo de las partículas detectadas es obtenido midiendo el retardo entre la señal del *trigger*, proporcionada por el detector T0, y la señal del TOF.

0.3 Resultados

Usando las ventajas en identificación de partículas de los detectores TPC y TOF, el mesón ϕ puede ser reconstruido a partir de los productos de su decaimiento. Este trabajo se enfocó en el canal de decaimiento a dos kaones: $\phi \rightarrow K^+ + K^-$.

0.3.1 Selección de Eventos y de Trazas

Se analizó en esta tesis los eventos de colisiones p-Pb a una energía de $\sqrt{s_{NN}} = 5.02$ TeV. Debido al diseño del magneto 2-en-1 del LHC, la energía de los dos haces no puede ser ajustada de manera independiente, llevando esto a diferente energía por beam. El sistema centro de masa está entonces desplazado con respecto al sistema de laboratorio con una rapidez de y_N = -0.465 en la dirección del haz del proton.

Los eventos seleccionados a analizar son aquellos que pasan algunos cortes estándar. Los eventos son aceptados si tienen vértice primario reconstruido en el detector SPD y cuya coordenada z se encuentre entre ±10 cm del punto de interacción. La multiplicidad en los eventos es obtenida en terminos del porcentaje del estimador de multiplicidad proporcionado por el detector V0A (lado del Pb).

[1] El gas contenido en el TOF es una mezcla de: $C_2H_2F_4(90\%)$,$i-C_4H_{10}(5\%)$, $SF_6(5\%)$

Se seleccionaron trazas primarias, que son aquellas producidas en la colisión incluyendo productos de decaimientos electromagnéticos débiles pero excluyendo productos de decaimientos débiles y particulas secundarias. Una partícula de decaimiento débil es una partícula hija de un decaimiento débil de un hadron ligero o de un muon.

0.3.2 Espectro de momento del mesón $\phi(1020)$

Como ya se mencionó, los mesones $\phi(1020)$ son identificados por su canal de decaimiento a dos kaones, los cuales son identificados mediante el uso de los detectores TPC y TOF. Como parte de la información obtenida es la energía(E) y el momento(p) de cada kaon, con esto se puede calcular la masa invariante de un par de kaones de la siquiente manera:

$$M_{inv}^2 = (p_1^2 + p_2^2) = (E_1 + E_2)^2 - (\mathbf{p_1} + \mathbf{p_2})^{\mathbf{2}} \tag{1}$$

Las distribuciones de masa invariante obtenidas tienen una seal alrededor de 1.02 GeV/c junto con una gran cantidad de ruido combinatorio proveniente de kaones no correlacionados. Este ruido se elimina mediante el método de eventos mixtos. La masa invariante de eventos mixtos se calcula a partir de kaones de carga opuesta de diferentes eventos, de tal manera que el pico de la seal no se formará pero si el ruido combinatorio.

Después de tener la distribucion de masa invariante, en la que el ruido combinatorio se sustrajo, es posible que ruido residual esté presente todavía. Entonces se ajusta una función *Voigt* para la region del pico o de la seal del ϕ y una función polinomial para describir el ruido residual. A partir de integrar la función de *Voigt*, sobre un amplio rango de masa, se obtiene el yield. Este procedimiento se repite para 15 rangos de momento transverso p_{T}, entonces se obtiene una distribución del yield de la ϕ en función de p_{T}. Se tiene una distribución semejante para cada intervalo de multiplicidad: 0-5%, 5-10%, 10-20%, 20-40%, 40-60%, 60-80% y 0-100%.

A cada espectro de producción, o yield, de la ϕ se tiene que corregir por algunos factores y correcciones que se relacionan con caracteristicas del detector. El principal es la corrección por eficiencia, en donde se toma en cuenta la imperfecta detección de todas las partículas provenientes de la colision. A partir de simulaciones Monte Carlo usando en particular el generador DPMJET, la eficiencia se calcula como el cociente siguiente:

$$\epsilon_{rec} = \frac{\phi_{reconstruido,TPC-TOF}}{\phi_{generado}}, \quad \text{donde} \tag{2}$$

- **Generado ϕ:** Son los mesones ϕ generados de eventos que cumplen los cortes ya antes descritos, y que no tienen interacción con los sistemas de detección, en este trabajo seria el caso de los detectores TPC y TOF.

- **Reconstruido ϕ:** Se refiere al numero de mesones ϕ para el cual sus dos kaones hijas en las que decayó son recontruidas dentro de la TPC o del TOF.

Para obtener es espectro de la partícula ϕ se usa la siguiente expresión:

$$\frac{d^2N}{\mathrm{dp_T}dy} = \frac{\mathrm{d}^2N_{raw}}{\mathrm{dp_T}dy} \cdot \frac{\varepsilon_{trig}}{\varepsilon_{rec}\varepsilon_{PC}} \tag{3}$$

donde

- ε_{rec} : Es la eficiencia de reconstrucción.

- ε_{PC} : Es la corrección de la seal, la cual toma en cuenta el numero de mesones ϕ que caen fuera de la región de integración.

- ε_{trig} : Corrección que toma en cuenta la eficiencia del vértice y del trigger, tiene un valor de $97.8 \pm 1\%$ para mediciones Minimum Bias.

$$\frac{\mathrm{d}^2N_{raw}}{\mathrm{dp_T dy}} = \frac{Yield}{N_{evt} \times BR \times \mathrm{dp_T dy}} \tag{4}$$

0.3.3 Discusión de Resultados

Los espectros del mesón ϕ se obtuvieron en función de p_{T} para siete multiplicidades. Para obtener información de estos espectros es necesario ajustar alguna función de la cual podamos extraer parametros. En particular se buscó obtener el yield integrado(dN/dy), mediante el ajuste de la función de Levy-Tsallis a cada uno de los espectros de las multiplicidades, de este ajuste. También se pudo obtener el p_{T} promedio ($\langle p_{\mathrm{T}} \rangle$). Se encontó una tendencia creciente para dN/dy para el ϕ, llendo de las colisiones mas perifericas a las mas centrales.

El $\langle p_{\mathrm{T}} \rangle$ se comparó con colisiones pp y con otros hadrones tales como: $(\mathrm{K}^{*0}, \Lambda, p, \mathrm{K}^{\pm}, \pi^{\pm})$. Similar a lo que se encontró en colisiones Pb-Pb, el $\langle p_{\mathrm{T}} \rangle$ tiene una tendencia creciente como función de la multiplicidad. Se esperaría que el comportamiento entre los hadrones K^{*0}, p, ϕ y Λ fuera el mismo, sin embargo, se obtuvo que siguen una gerarquía aparente de masas.

Se comparó la producción del mesón ϕ con la producción de K, π, p, en función de la multiplicidad y para collisiones pp y Pb-Pb. El comportamiento de los resultados en p-Pb es compatible con Pb-Pb, y pp, además de que la prediccion del Modelo Termal concuerda con los resultados más centrales.

Las diferencias en los mecanismos de producción de bariones y mesones pueden ser estudiados en las razones barión-mesón. Si la producción de hadrones puede ser explicada en terminos de hidrodinámica, entonces las masas de las particulas juega un rol importante en determinar la forma de las distribuciones de p_{T}. Para estudiar este aspecto, la distribución de p_{T} del mesón ϕ es comparada con la de los protones, el cual es un barion de masa similar pero diferente contenido de quarks. En las razones p/ϕ como funcion de p_{T} muestran una tendencia decreciente tanto en colisiones perifericas y centrales. Las colisiones pp y Pb-Pb(80-90%) tienen un excelente acuerdo con las perifericas en Pb-Pb, mientras que (0-5%) en p-Pb es intermedio entre pp y Pb-Pb(0-10%).

En la razón ϕ/π una tendencia creciente y muy semejante entre colisiones perifericas(60-80%) y centrales(0-5%). Si comparamos con la razon barión-mesón p/π en p-Pb y en Pb-Pb, vemos que son comportamientos crecientes muy parecidos. Esto indicaría que el numero de quarks no es un factor importante que determine las distribuciones de p_{T} de las particulas en bajo y p_{T} intermedio, para colisiones centrales.

0.4 Conclusiones

En este trabajo se midió la producción del mesón ϕ en colisiones p-Pb a una energía de $\sqrt{s_{NN}} = 5.02$ TeV, en la región de rapidez $-0.5 < \mathrm{y} < 0$. Se estudió el canal de decaimiento a dos kaones, el cual tiene una probabilidad de decaimiento del 48.9%. Mediante el uso de las capacidades de identificación de partículas de los detectores TPC y TOF los kaones fueron seleccionados y calculandose así la masa invariante. El ruido combinatorio es sustraido de las distribuciones de masa invariante mediante la técnica de Eventos Mezclados. La producción del mesón ϕ se obtuvo mediante el conteo de las entradas en la distribución de masas invariantes, después se aplicaron correcciones y factores de normalización para obtener el espectro de p_{T} del mesón ϕ para eventos divididos en siete multiplicidades, la cual es medida por el detector V0A.

Al espectro del ϕ se ajusta una función Levy-Tsallis para obtener la producción integrada (dN/dy) y p_{T} promedio. Que después se comparan con los valores de otras partículas más estables (p, K, π). Se encontró que el $\langle p_{\mathrm{T}} \rangle$ tiene una tendencia creciente, en función de

multiplicidad, y que aparentemente se sigue una jerarquía de masas en los casos de p, K^{*0} y ϕ. El mismo comportamiento esta presente en colisiones pp.

Las razones ϕ/p como función de p_T para colisiones p-Pb perifericas (60-80%) es compatible con los resultados de pp y Pb-Pb(80-90%). Para colisiones p-Pb centrales (0-5%) los valores de la razón son intermedios entre colisiones centrales y perifericas de Pb-Pb, comportamiento que era esperado. Por el otro lado, en la razón mesón-mesón ϕ/π prácticamente no hay diferencia entre los valores de colisiones centrales y perifericas p-Pb. Una tendencia creciente semejante se presenta en p/π para Pb-Pb, entonces podemos concluir que la masa de las partículas es un parametro importante y no tanto el contenido de quarks.

List of Figures

Chapter 1

High Energy Physics

1.1 Standard Model

The High Energy Physics(HEP) has established and tested since the 60's a detailed theory of the elementary particles and their fundamental interactions called Standard Model. The Standard Model describes the fundamental forces and the composition of matter. It is a gauge theory that includes the strong, weak, and electromagnetic forces and the related interactions. Being the gravity the fourth force that is not included in this theory. According to the Standard Model theory, all mater is constituted out of point-like particles which have a spin 1/2 and grouped into three families, each family has two quarks and two leptons members [1].

The $SU(3) \times SU(2) \times U(1)$ Standard Model(SM) is the combination of three theories, describing each of the forces. The Quantum Chromodynamics (QCD) is one of the components of the SM(SU(3)), it is a gauge theory which describes the strong interactions of colored quarks(q) and gluons(g). The color is a property similar to the charge in strong interactions, for example, a quark of specific flavor can have three different color charge (green, blue and red) and in order to form hadrons which are colorless(white), either with three colored quarks or a quark and an anti-quark. Hadrons are grouped into baryons and mesons. Baryons consist of three quarks, qqq or $\overline{qqq}$ while mesons consist of two quarks ($q\overline{q}$). The gluons are the mediators of the strong force. The interaction between quarks and gluons can change the color but not the flavor. Since color (like electric charge) is always conserved, this means that the gluon come in eight different bi-colored combinations [1].

The electro-weak interaction is based on the gauge theory group $SU(2) \times U(1)$. There

are two kinds of electro-weak interactions: charged(mediated by $W^{\pm}$) and neutral(mediated by Z^0), the first one is the only that changes flavor. The Quantum Electrodynamics(QED) describes the electromagnetic interactions mediated by the exchange of photons(γ). Leptons are affected by the weak force and the charged ones in addition by electromagnetic force.

The Standard Model has also, however, limitations that require extensions to keep the theory consistent. The most important issue is the masses of the electro-weak gauge bosons predicted to be zero within the theory. This is clearly inconsistent with experiment. This situation can be resolved by an additional gauge boson added to the theory, the Higgs boson. The Higgs mechanism generates the masses for the $W^{\pm}$ and the Z^0 while the γ remains massless. Recent results from LHC have confirmed, in July 2012, the existence of a unknown particle with a mass between 125 and 127 GeV/c^2. By March 2013, the particle has been proven to behave, interact and decay in many of the ways predicted by the Standard Model, and was also tentatively confirmed to have positive parity and zero spin, two fundamental attributes of a Higgs boson [2].

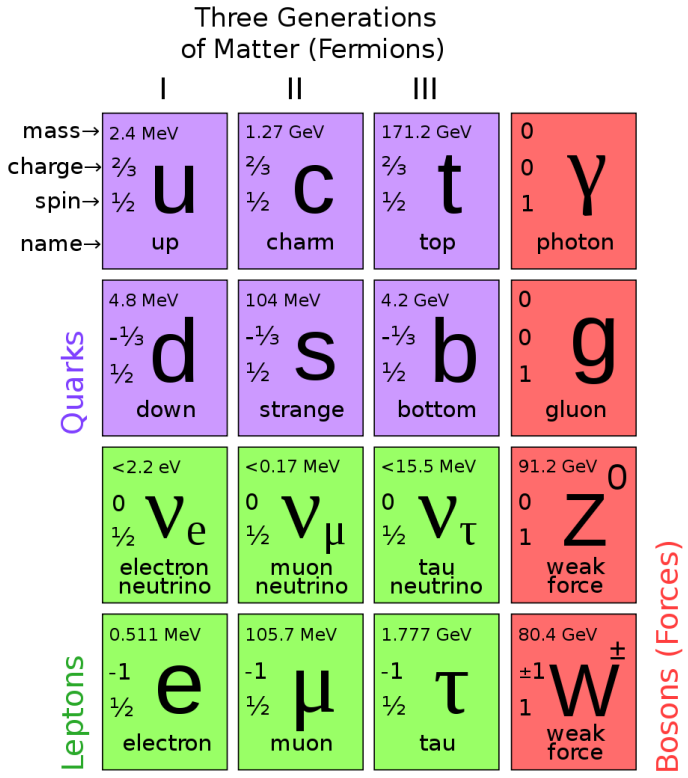

Figure 1.1: Fundamental particles and the forces mediators.

1.2 Kinematic Variables

In order to analyse and measure the properties of the hadrons, it is convenient to define some variables that depend on some measurable quantities of the particles. The energy-momentum four-vector is:

$$p^{\mu} = (p^0, p^1, p^2, p^3) = (E/c, p_x, p_y, p_z) \tag{1.1}$$

The transverse momentum is defined in terms of the p_x and p_y components of the total momentum p.

$$p_T = \sqrt{p_x^2 + p_y^2}, \tag{1.2}$$

then the energy-momentum four-vector can be written as $p^{\mu} = (E, p_T, p_z)$ where c=1. In the figure 1.2, left image, it is shown the momentum vector over the x-z plane, where θ_{cms} is the direction of the vector with respect to z-axis (beam axis) and the right image shows the transverse momentum vector in the x-y plane [3].

The rapidity(y) is defined as a function of the energy(E) and the longitudinal momentum(p_z) of the same particle, the expression is:

$$y = \frac{1}{2} ln \frac{E + p_z}{E - p_z} \tag{1.3}$$

If one considers the case in which the momentum magnitude of a particle is much bigger than the mass of the same particle, i.e. $p \gg m$, the rapidity(y) can be approximated as $y \approx -ln[tan(\theta/2)]$ where θ is the vector momentum angle with respec to the beam axis (z direction). Under this approximation the rapidity is known as pseudorapidity[3].

$$\eta = -ln[tan(\theta/2)] \tag{1.4}$$

The figure 1.2 shows examples of the different values of the pseudorapidity and its corresponding angle in the x-z plane.

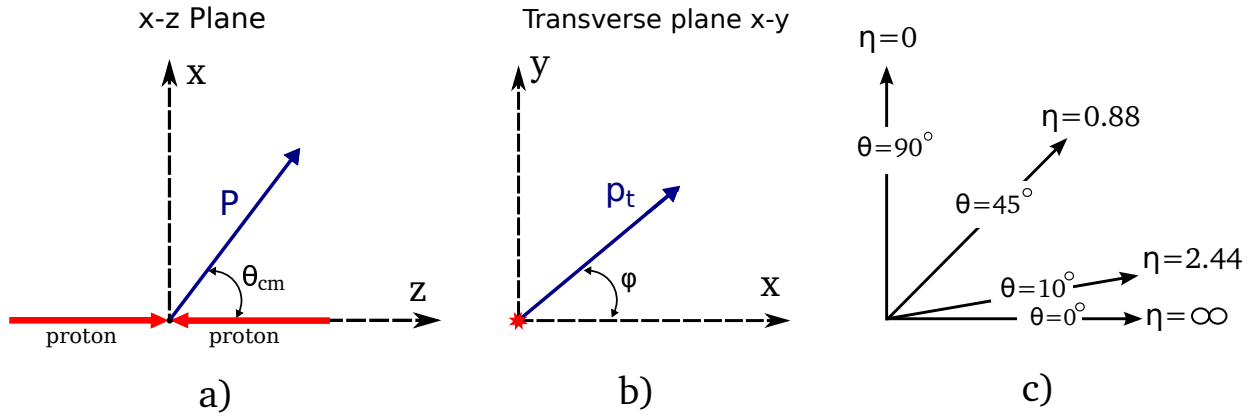

Figure 1.2: a) The momentum vector in the plane x-z, b) Transverse plane, where p_{T} is measured, c) Illustrative values for the pseudorapidity and their respective θ angle values.

1.3 Quantum Chromodynamics (QCD)

The QCD is the theory of the strong interactions. The strong interactions have been studied since the beginning of the 20th century soon after the discovery of the atomic nucleus. This interaction is a fundamental force describing interactions between quarks and gluons which make up hadrons (protons, neutron, pions, etc), similar description to the way QED does for electrons and photons. In QCD, the interactions are invariant under a SU(3) transformation in colour space (SU(3) colour symmetry). Thus, the quarks carry three colour charges, and each gluon is a combination of eight different combinations of colour and anti-colour charge. The intrinsic charge of the gauge field (the gluon) is the decisive modification in comparison to QED; it makes the pure gluons system self-interactive, in contrast to the ideal gas of photons[13]. The two main strong interaction features of interest for heavy-ion physics are:

- **Colour confinement:** the force between quarks does not diminish as they are separate. Because of this. When one tries to separate two quarks, the energy is enough to create another quark and then creating another quark pair; they are forever bound into hadrons such as the proton and the neutron or the pion and kaon. Although analytically unproven, confinement is widely believed to be true because it explains the consistent failure of free quark searches, and it is easy to demonstrate in lattice QCD.
- **Asymptotic freedom:** the value of the strong coupling constant, α_S, depends on the momentum transfer (Q^2) at which an observed process occurs (running coupling

constant). α_S decreases with increasing energy and asymptotically, at infinite energy, tends to zero .

There is no known phase-transition line separating these two properties; confinement is dominant in low-energy scales but, as energy increases, asymptotic freedom becomes dominant. This theory predicts that strong interaction properties in a complex system may differ from those observed in the vacuum. Quark confinement inside hadrons can disappear at energy densities higher than those typical of normal nuclear matter [13].

The Lagrangian density of QCD is given by [4]:

$$L = -\frac{1}{4}F^a_{\mu\nu}F^{\mu\nu}_a + \sum_f \overline{\psi}^f_\alpha (i\gamma_\mu D^\mu)\overline{\psi}^f_\beta \tag{1.5}$$

with the non Abelian group tensor

$$F^a_{\mu\nu} = (\partial_\mu A^a_\nu - \partial_\nu A^a_\mu - g f^a_{bc} A^b_\mu A^c_\nu) \tag{1.6}$$

and

$$D_\mu = \partial_\mu + ig\frac{\lambda_a}{2}A^a_\mu \tag{1.7}$$

The fundamental degrees of freedom of the theory are the 3×6 quarks fermionic fields ψ and the eight gluonic fields A_μ. λ_a and f^a_{bc} are the eight $SU(3)$ group generators (the 3×3 Gell-Mann matrices) and the structure constants.

The inclusion of quark masses would add a term

$$L_m = \sum_f m_f \overline{\psi}^f_\alpha \psi^{f\alpha} \tag{1.8}$$

in Eq. 1.5. Equation 1.7 contains one dimensionless coupling constant g, and hence Eq. 1.5 provides no scale: QCD predicts only the ratios of physical quantities, not absolute values in terms of physical units. In QCD hadrons are colour-neutral bound states of quarks (baryons) or of quark-antiquark pairs (mesons); they are thus the chromodynamic analogue of atoms as the electrically-neutral bound states in QED. The differences between the two theories becomes significant at large distances: while a finite ionization energy ΔE suffices to break up the electrodynamic bound, this is not possible in the case of quark binding. This property of the QCD leads to the concept of "confinement". At short distances QCD shows another peculiar behaviour, the decrease of the colour charge with decreasing the

distance from the colour-probe to the charge itself. This leads to the concept of "asymptotic freedom", which implies that partons[1] inside hadrons interact weakly among themselves and can be considered as almost free.

1.4 Quark Gluon Plasma (QGP)

Ultra-relativistic heavy ion collisions offer a good opportunity to investigate highly excited dense nuclear matter under controlled laboratory conditions. The aim for such studies is the expectation that an entirely new form of matter may be created from such reactions. That form of matter, called Quark Gluon Plasma (QGP), is the QCD analogue of the plasma phase of ordinary atomic matter. Nevertheless, the deconfined quanta of a QGP are not directly observable because of the fundamental confining property of the physical QCD vacuum. What is observable are hadronic and leptonic residues of the transient QGP state. Among some probes there are the Leptonic probes, $\gamma, e^+e^-, \mu^+\mu^-$, they carry information about the spectrum of electromagnetic current fluctuations in the QGP stat; the abundance of quarkonia $\Psi, \Psi', \Upsilon, \Upsilon'$ (also observed via l^+l^-) carry information about the chromoelectric field fluctuations in the QGP. The large number of hadronic probes, $\pi, K, p, \overline{p}, \Lambda, \Xi, \Omega, \phi, \rho, ...$ provide information on the quark flavor chemistry and baryon number transport. Theory suggest that with decays such as $\rho \rightarrow e^+e^-$ the properties of the hadronization and chiral symmetry breaking can be indirectly studied. Quantum statistical interference patterns in $\pi\pi, KK, pp, \Lambda\Lambda$ correlations provide somewhat cloudy lenses with which the space-time geometry of hadronic ashes of the QGP can be investigated. The detailed rapidity and transverse momentum spectra of hadrons provide barometric information of pressure gradients during the explosive expansion of the QGP medium[5].

The main problem with all the above probes is precisely that they are all indirect messengers. Since we can not see free quarks and gluons it is not trivial to verify the QCD predictions of the QGP state. However, nature choses to hide those constituents within the confines of colour neutral composite many body systems hadrons.

1.4.1 Phases of strongly interacting matter

It is expected that in heavy ion collisions, one reaches conditions under which the structured confining vacuum is dissolved, forming a domain of thermally equilibrated hadronic matter

[1] The basic constituents of hadrons, quarks and gluons.

comprising freely moving quarks and gluons. A schematic plot of the the phase diagram of dense hadronic matter is shown in figure 1.3 The different phases populate different domains of temperature T and baryon density. For high temperatures and/or high baryon density, we have the deconfined phase. If deconfinement is reached in the nuclear-collision, it freezes back into the state containing hadrons during the temporal evolution of the small *fireball*. The most difficult domain to reach experimentally is the one of low baryon number density, at high T, corresponding to the conditions that were in the early Universe. This demands extreme collision energies, which would permit the baryon number to escape from the central rapidity region, where only the collision energy is deposited.

Now we want to qualitatively understand the magnitude of the temperature at which the deconfined quark-gluon phase will freeze into hadrons. The order of magnitude of this transition temperature (if a phase change occurs) or cross temperature (if no phase transition occurs) is obtained by evaluating where a benchmark value for energy density occurs, $\varepsilon_H \approx 3P_H = 1$ GeV fm^{-3} [6]. The generalized Stefan-Boltzmann law describes the energy density ε and pressure P as functions of the temperature T of a massless relativistic gas:

$$P^{SB} = \frac{1}{3}\varepsilon^{SB} = \frac{\pi^2}{90} g T^4 \tag{1.9}$$

where the quantity g is the number of different (relativistic) particle states available and is often called the 'number of degrees of freedom' or 'degeneracy'. In the deconfined phase,

$$g \equiv g_g + \frac{7}{4} g_q, \tag{1.10}$$

which comprises the contribution of massless gluons(bosons) and quarks(fermions). The relative factor $2 \times \frac{7}{8} = \frac{7}{4}$ expresses the presence of particles and antiparticles (factor 2) and the smaller fermion phase space, compared with the boson case, given the exclusion principle. Gluons and quarks carry color and spin, but quarks in addition come in two($n_f = 2$) flavors u and d. Since at high temperatures the flavor count may include the strange quark, we leave ($n_f = 2$) as a variable. Then we obtain the following degeneracy in a QGP:

$$\begin{aligned} &gluons : g_g = 2(spin) \times (N_c^2)(color) = 2 \times 8 = 16, \\ &quarks : g_q = 2(spin) \times N_c(color) \times n_f(flavor) = 2 \times 3 \times n_f. \end{aligned}$$

When the semi-massive strange quarks are present, the effective number of 'light' flavors is

≈ 2.5. Thus, $g \approx 40$ in equation 1.9, to be compared with just two directions of polarization for photons[6].

For a massless ideal quark-gluon gas, we find

$$T_H = 160MeV, \quad \text{for} \quad \varepsilon_H = 1.1 \text{ GeVfm}^{-3}$$

Hagedorn introduced this critical temperature in his study of the boiling point of hadronic matter[29].

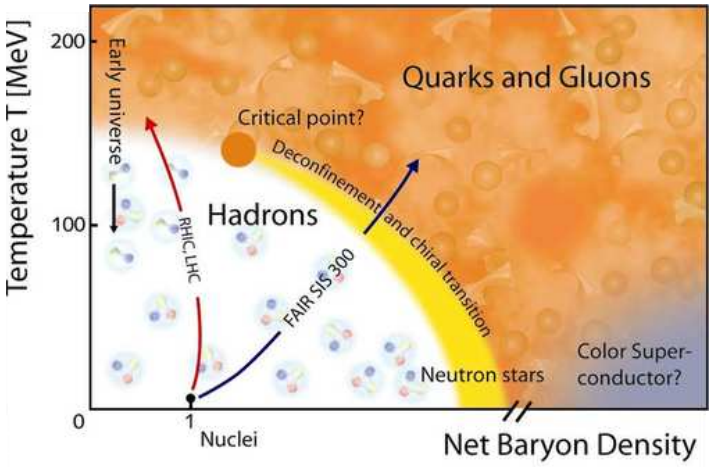

Figure 1.3: Regions of the principal forms of hadronic matter are shown in the baryon-density-temperature plane.

1.4.2 Strangeness enhancement

The quarks u and d from which the stable matter is made are easily produced as quark-antiquark pair because they have small masses. Another abundantly added quark flavor is strangeness, particularly if the deconfined QGP phase of matter is formed. Strangeness was one of the first proposed signatures of the deconfined phase. The mass of strange quarks and antiquarks is of the same magnitude as the temperature T at which protons, neutrons, and other hadrons are expected to dissolve into quarks. This means that the abundance of strange quarks is sensitive to the conditions, structure, and dynamics of the deconfined-matter phase.

In proton proton collisions, the production of particles containing strange quarks is strongly suppressed as compared to the production of particles with u and d quarks [7].

It has been argued that this suppression is due to the higher mass of the $s\overline{s}$ quark pair. The suppression increases with the strangeness content of the particles produced in proton proton collisions.

In case of QGP formation, $s\overline{s}$ pairs can either be produced via the interactions of two gluons or of $q\overline{q}$ pairs. Leading order α_s pQCD calculation suggest that the second process dominates only for $\sqrt{s} \leq 0.6$ GeV. The time-scale of chemical equilibration of (anti-) strangeness due to gluon gluon interaction is estimated to be about 3 to 6 fm/c, depending on the temperature of the plasma[8]. Following this line, the yield of strange and multi-strange mesons and baryons has been predicted to be strongly enhanced in the presence of a QGP as compared to a purely hadronic scenario at the same temperature. However, the estimated equilibration times may not be sufficient rapid to cause a saturation in the production of strange hadrons before QGP freeze-out. Some examples of strange particles are listed below:

- **Cascades $\Xi(qss)$:** The doubly strange cascades, $\Xi^0(uss)$ and $\Xi^-(dss)$, are below the mass threshold for hadronic decays into hyperons and kaons. Consequently, there is only one decay in each case, $\Xi^0 \to \Lambda + \pi^-$ ($c\tau = 4.9cm$) and $\Xi^0 \to \Lambda + \pi^0$ ($c\tau = 8.7cm$). There are also several Ξ^* resonances known, which normally feed down in a hadronic decay into the hyperon and kaon abundances: $\Xi^*(qss) \to Y(qqs) + \overline{K}(\overline{q}s)$.

- **Omegas $\Omega^-(qss)$:** There are several primary weak-interaction decay channels leading to the relatively short proper decay path, ($c\tau = 2.46cm$): $\Omega^-(1672) \to \Lambda + K^-$ (68%), $\Omega^-(1672) \to \Xi^0 + \pi^-$ (24%) and $\Omega^-(1672) \to \Xi^- + \pi^0$ (9%). The first of these decay channels is similar to the decay of the Ξ^-, except that the pion is replaced by a kaon in the final state. In the other two options, after cascading has finished, there is a neutral pion in the final state, which makes the detection of these channels impractical.

- **Phi $\phi(s\overline{s})$:** The species addressed in this thesis, the vector (J=1) meson ϕ is believed to be a 'pure' bound state of the strange-quark pair $\phi = s\overline{s}$. With mass 1019.45 MeV, it has a relatively narrow full width $\Gamma_\phi = 4.26$ MeV. The main two decay channels are:

$$\phi \to K^+ + K^-, \quad 48.9\%$$
$$\phi \to K^0_L + K^0_S, \quad 34.2\%$$

1.4.3 Resonances

Hadronic resonances have their importance in high energy collisions analyses because they can provide experimental evidence for partial chiral symmetry restoration in the deconfined Quark-Gluon phase produced in this energetic collisions. The production of resonances occurs both during the transition (at a critical temperature $T \approx 160$ MeV) from the quark-gluon plasma (QGP) to the hadronic phase and in the hadronic phase itself by regeneration. Since the resonances lifetimes are comparable to the lifetime of the partonic plasma phase (a few fm/c) they are an important tool to investigate medium modifications to the resonant state due to chiral transition[9]. It is expected that chiral symmetry is restored at around the same critical temperature as the deconfined phase transition, with the quark-antiquark condensate decreasing towards 0 with increasing temperature. Resonances that interact with the medium in the mixed or early hadronic phase, when chiral symmetry is at least partially restored, may be shifted of their mass and exhibit broader widths than observed in vacuum[10].

The temperature evolution and lifetime of the hadronic phase affect the relative strengths of resonance-generation processes and re-scattering, and therefore ratios of resonance yields to non-resonance yields. Particle ratios have been predicted as functions of the chemical freeze-out temperature and the elapsed time between chemical and thermal freeze-out using thermal models[10]. In principle, measurements of two different particle ratios are needed to tune the thermal models and determine uniquely the chemical freeze-out temperature and the lifetime of the hadronic medium.

The study of the mesonic resonances $\phi(1020)$ and $K^{*0}(892)$ production is of particular interest. They have mass close to the proton mass but their lifetimes differ of about a factor of 10, being $\tau_\phi = 46$ fm/c and $\tau_{K^{*0}} = 4.0$ fm/c, and their strangeness content differ by one unity. The K^{*0} is expected to be more sensitive to the re-scattering effects in the hadronic medium because of the much shorter lifetime. The ϕ is other story because it can escape the medium with almost no re-scattering, then this resonance is a good candidate to investigate partial restoration of chyral symmetry at the formation time. In addition, the ϕ can help to probe strangeness production, being the lightest vector meson composed of sea quarks ($s\overline{s}$). In pp collisions, $s\overline{s}$ pair production was found to be significantly suppressed with respect to $u\overline{u}$ and $d\overline{d}$[15].

Chapter 2

The ALICE Experiment at LHC

2.1 Large Hadron Colider

The LHC is, at the moment, the biggest particle accelerator in the world. The idea of the project started in 1984, was approved in 1994 and the construction work in the underground tunnel started in 2001. Before the LHC, CERN[1] had the LEP[2] that was working from 1989 to 2000. Then after dismantling of the LEP, the LHC used the same underground tunnel of 27 km of circumference. The LHC is located under the the Swiss-French border area close to Geneva at a depth of 50 to 175 m.

The LHC is a synchrotron that accelerates two counter-rotating beams in separate beam pipes. Each beam rotates several times around the ring until it reach enough energy to collide. The largest achievable acceleration energies are 7 TeV for protons and 2.76 TeV per nucleon for lead ions, therefore providing collisions at $\sqrt{s} = 14$ TeV and $\sqrt{s} = 5.5$ TeV, respectively.

To keep the beam focused and to bend the beam through the ring, the LHC has 1232 dipoles of 14.3 m length and contains superconducting magnets which operate at a temperature of 1.9 K. And 392 quadrupoles maintain the beam focused, each quadrupole has a length between 5 and 7 m. Powered by a maximum current of 11.7 kA the dipoles can provide a magnetic field from 0.535 T during the injection (beam energy of 450 GeV) up to 8.33 during the collisions(energy of 7 TeV) [11].

[1] Centre Européen pour la Recherche Nucléaire.
[2] Large Electron Positron Collider

2.1.1 The accelerator complex

The accelerator complex at CERN is a succession of machines that accelerate particles to increasingly higher energies. Each machine boosts the energy of a beam of particles, before injecting the beam into the next machine in the sequence. In the Large Hadron Collider (LHC) the last element in this chain particle beams are accelerated up to an energy of 4 TeV per beam. Most of the other accelerators in the chain have their own experimental halls where beams are used for experiments at lower energies. The proton source is a simple bottle of hydrogen gas. An electric field is used to strip hydrogen atoms of their electrons to yield protons. Linac 2, the first accelerator in the chain, accelerates the protons to the energy of 50 MeV. The beam is then injected into the Proton Synchrotron Booster (PSB), which accelerates the protons to 1.4 GeV, followed by the Proton Synchrotron (PS), which pushes the beam to 25 GeV. Protons are then sent to the Super Proton Synchrotron (SPS) where they are accelerated to 450 GeV. The protons are finally transferred to the two beam pipes of the LHC. The beam in one pipe circulates clockwise while the beam in the other pipe circulates anticlockwise. It takes 4 minutes and 20 seconds to fill each LHC ring, and 20 minutes for the protons to reach their maximum energy of 4 TeV. Beams circulate for many hours inside the LHC beam pipes under normal operating conditions. The two beams are brought into collision inside four detectors ALICE, ATLAS, CMS and LHCb where the total energy at the collision point is equal to 8 TeV. The accelerator complex includes the Antiproton Decelerator and the Online Isotope Mass Separator (ISOLDE) facility, and feeds the CERN Neutrinos to Gran Sasso (CNGS) project and the Compact Linear Collider test area, as well as the neutron time-of-flight facility (nTOF). Protons are not the only particles accelerated in the LHC. Lead ions for the LHC start from a source of vaporized lead and enter Linac 3 before being collected and accelerated in the Low Energy Ion Ring (LEIR). They then follow the same route to maximum energy as the protons.

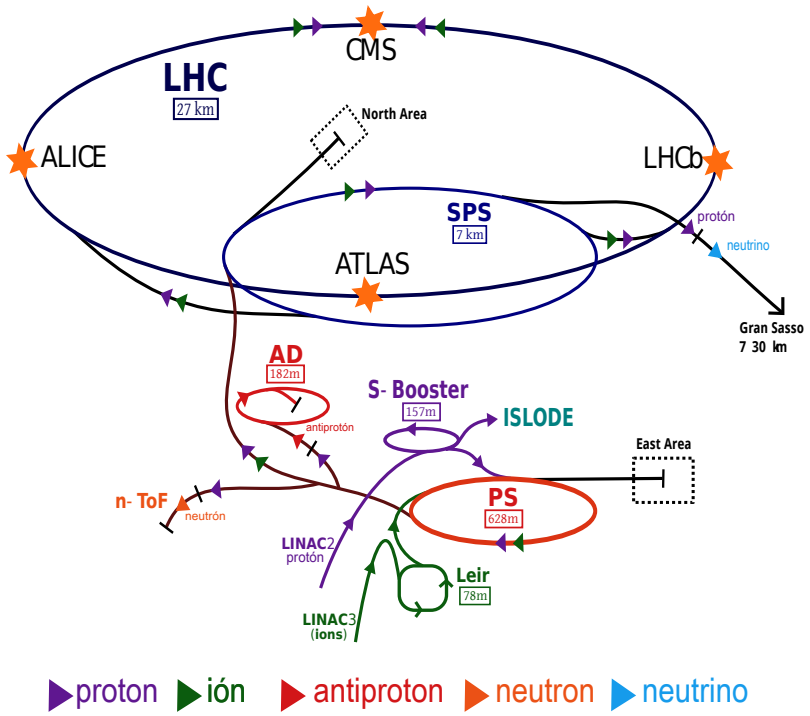

Figure 2.1: Distributions of the CERN's accelerators that increase the energy of the protons up to 7 TeV.

2.2 ALICE (A Large Ion Collider Experiment)

The ALICE, one of the four big experiments at CERN and the one in which this thesis is focused, is 16 m high, 26 m length and has a total weight around 10,000 t. It is designed to address the physics of strong interacting matter and the quark-gluon plasma at extreme values of energy density and temperature in nucleus-nucleus collisions. ALICE will allow the comprehension of hadrons, electrons, muons, and photons produced in the collision of heavy nuclei (Pb-Pb). The physics programme also includes collision with lighter ions and at lower energy, in order to vary energy density and interaction volume, as well as dedicated proton-nucleus runs[18]. Proton-proton runs recorded in ALICE will provide reference data for the heavy-ion programme and address a number of specific strong-interaction topics for which ALICE is complementary to the other LHC detectors. The ALICE physics programme is summarized below:

- pp collisions at $\sqrt{s} = 900$ GeV and 7 TeV during 2010

- PbPb collisions at $\sqrt{s} = 2.76$ TeV in November 2010
- pp collisions at $\sqrt{s} = 7$ TeV during 2011
- PbPb collisions at $\sqrt{s} = 2.76$ TeV in Autumn 2011
- LHC technical stop in 2012
- pp collision at $\sqrt{s} = 14$ TeV starting from 2013 and then regular runs
- Subsequent heavy-ion program:
  1-2 years PbPb
  1 year pPb-like collision (pPb,dPb or αPb)
  1-2 years Ar-Ar

Among some physics observables that ALICE can study are the global event structure such as multiplicity and transverse or zero-degree energy flow. With this is possible to define the geometry, i.e. impact parameter, shape and orientation of the collision volume, and number of interacting nucleons. Nuclear modification to the parton distribution function can be extracted by comparing global event features and, more directly, specific hard processes like direct photons, heavy flavours in pp, pA and A-A collisions.

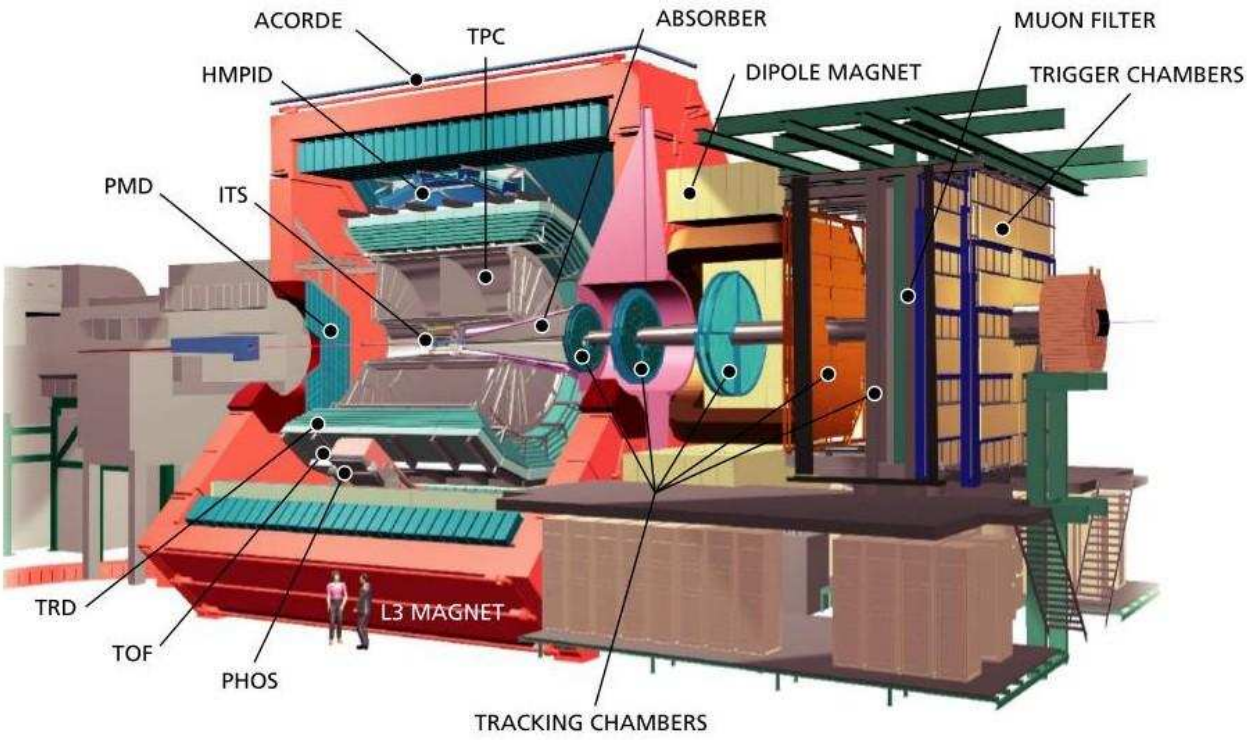

Figure 2.2: ALICE schematic layout.

2.2.1 ALICE detectors

ALICE consists of an ensemble of several detectors, it has the central barrel part which measures hadrons, electrons, and photons, and a forward muon spectrometer. The central part cover polar angles from 45° to 135° and is embedded in a large solenoid magnet. From inside out, the barrel contains an Inner Tracking System (ITS) of six planes of high-resolution silicon pixel (SPD), drift (SDD), and strip (SSD) detectors, a cylindrical Time-Projection Chamber (TPC), three particle identification arrays of Time-of-Flight (TOF), Ring Imaging Cherenkov (HMPID) and Transition Radiation (TRD) detectors, and two calorimeters (PHOS and EMCal). Excepting HMPID, PHOS, and EMCal all the other detectors cover the full azimuthal angle.

VZERO

The V0 detector [16] is a small angle detector consisting of two arrays of scintillator counters, called V0A and V0C, which are installed on either side of the ALICE interaction point.

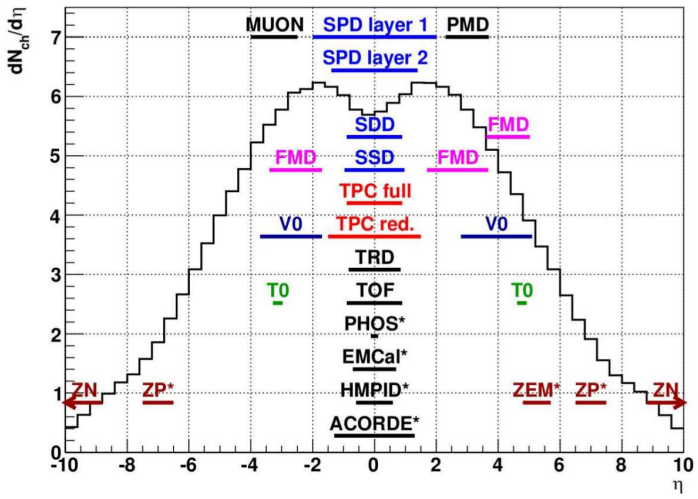

Figure 2.3: Pseudorapidity (η) ranges covered by ALICE detectors.

This detector has several functions. It provides minimum-bias triggers for the central barrel detectors in pp, pA and A-A collisions. These triggers are given by particles originating from initial collision and from secondary interactions in the vacuum chamber elements. As the dependence between the number of registered particles on the V0 arrays and the number of primary emitted particles is monotone, the V0 serves as an indicator of the centrality of the collision via the multiplicity recorded in the event.

The V0A detector is located 340 cm from the vertex on the side opposite to the muon spectrometer whereas V0C is fixed to the front face of the hadronic absorber, 90 cm from the vertex. They cover the pseudo-rapidity ranges $2.8 < \eta < 5.1$ (V0A) and $2.8 < \eta < 5.1$ (V0C) and are segmented into 32 individual counters each distributed in four rings.

Inner Tracking System (ITS)

The ITS is the closest detector to the beam axis. As shown schematically in figure 2.4 the ITS consist of six cylindrical layers of silicon detectors, located at a radii between 4 and 43 cm. ITS covers the rapidity range of $|\eta| < 0.9$ for al vertices located within the length of the interaction diamond ($\pm 1\sigma$, i.e. ± 5.3 cm along the beam direction). The number, position and segmentation of the layers were optimized for efficient track finding and high impact-parameter resolution. The two first layers correspond to the SPD[1] located at $r = 4$ and 7.2 cm respectively and a length of 28.2 cm along z axis. The next two layers correspond

[1]Silicon Pixel Detector

to SDD[1] with radii of $r = 15$ and 23.9 cm being the inner cylinder shorter than the outer one, 44.4 cm and 59.4 cm respectively. The last two layers, the SSD[2] with $r = 38.5$ and 43.6 cm [17].

The main tasks of the ITS are to localize the primary vertex with a resolution better than 100 μm, to reconstruct secondary vertices from the decays of hyperons and D and B mesons, to track and identify particles with momentum below 200 MeV/c, to improve the momentum and angle resolution for particles reconstructed by the Time Projection Chamber (TPC) and to reconstruct particles traversing dead regions of the TPC [19].

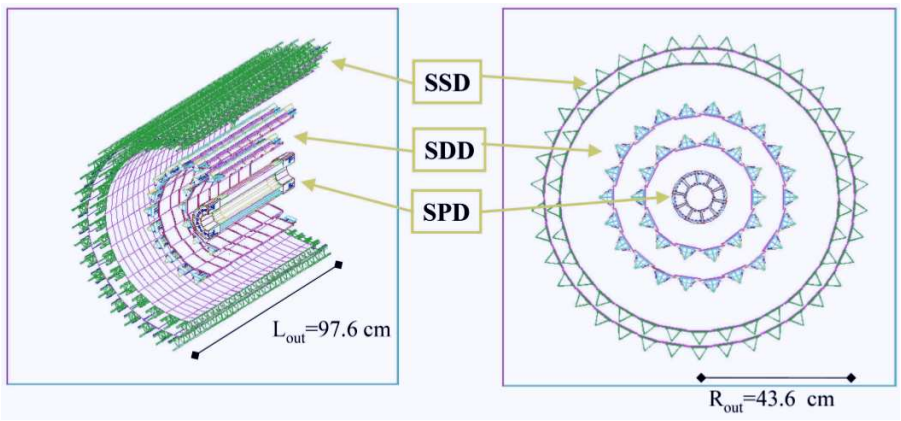

Figure 2.4: ITS detector dimensions and sub-detectors.

Time Projection Chamber (TPC)

The Time Projection Chamber is the main tracking detector of the central barrel and is optimised to provide, together with other central barrel detectors, charged particle momentum measurements with good two-track separation, particle identification, and vertex determination. In addition, data from central barrel detectors are used to generate a fast online High-Level Trigger (HLT) for the selection of low cross section signals. The TPC is a cylindrical detector with an inner radii of 84.8 cm and outer radii of 246.6 cm, covering 500 cm along the beam axis. The phase space covered by the TPC is $|\eta| < 0.9$ for tracks with full radial track length(matches in ITS, TRD, and TOF detectors). The TPC covers the full azimuth (with exception of the dead zones). A large p_{T} range is covered from about 0.1 GeV/c up to 100 GeV/c with good momentum resolution [19].

[1]Silicon Drift Detector
[2]Silicon micro-Strip Detector

This detector consist of two main parts: the field cage and the readout chambers. Both are filled with a gas mixture of Neon, Nitrogen and CO_2. If a charged particle travels through the gas volume, it excites and ionizes has atoms along its track. As a consequence, it loses an amount of energy per unit track length (dE/dx) which is specific for every particle type. Inside the field cage, a homogeneous electric field perpendicular to the readout chambers is generated: The cathode plane of the readout chambers is at a potential of 0V and, in the middle of the TPC, the parallel central electrode is set to a negative voltage of 100kV. At the borders of the field, the homogeneity of the field is achieved by special equipotential strips which are connected by a voltage divider. Thus, every strip is put to a potential that its center would have in a homogeneous field [23].

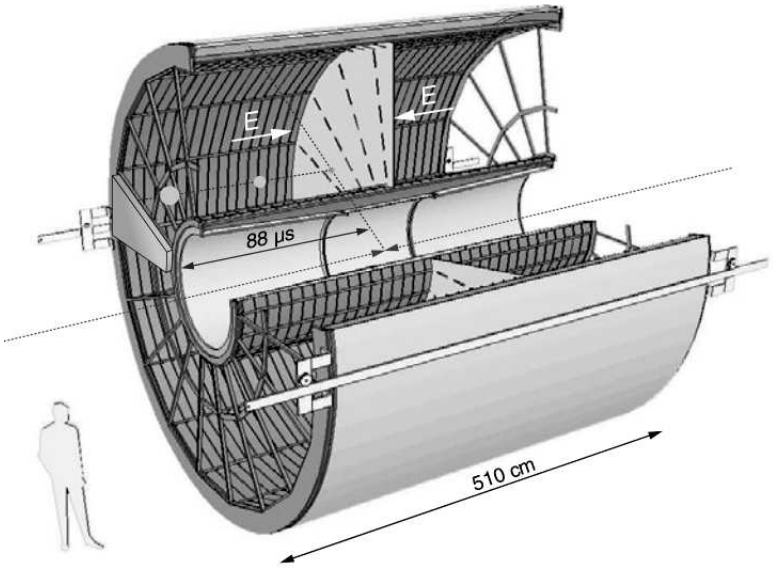

Figure 2.5: TPC detector dimensions.

The readout chamber is a multi-wire proportional chamber (MWPC) shown in figure 2.6. It is consisting of a segmented cathode pad plane and the anode, cathode and gating wire planes. The anode wires are set to a positive voltage of 1500V which leads to an amplification of the drifted electrons: In the vicinity of the wire the electric field grows proportional to 1/r. The electron energy rises which leads to ionization and the released electrons themselves cause an avalanche process [23].

TPC allows the three-dimensional reconstruction of the tracks. The pads provide the reconstruction of the coordinates (x,y) via the distribution of the induced signal. The position

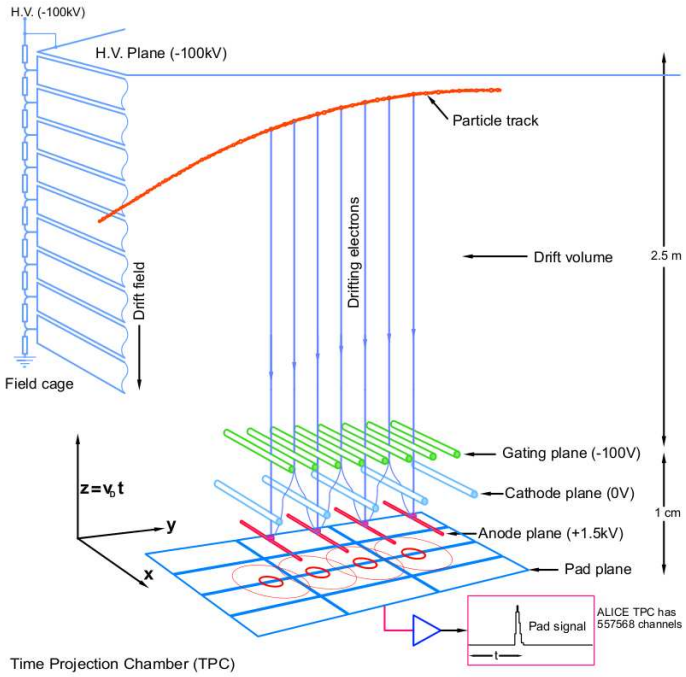

Figure 2.6: Schematic illustration of the working principle and the read-out chambers of the TPC.

of the particle in the drift direction is obtained with the measurement of the drift time (Δt) till the readout planes. The drift velocity of the electrons (v_e) in the gas is well known; then the coordinate z is calculated with $z = v_e \Delta t$. The three dimensional signal is called cluster.

Time Of Flight (TOF)

The Time-Of-Flight (TOF) detector is a large area array that covers the central pseudo-rapidity region ($|\eta| < 0.9$) for Particle IDentification (PID) in the intermediate momentum range, below about 2.5 GeV/c for pions and kaons, up to 4 GeV/c for protons, with a π/K and K/p separation better than 3σ. The TOF, coupled with the ITS and TPC for tracks and vertex reconstruction and for dE/dx measurements in the low-momentum range (up to about 1GeV/c), provides even-by-event identification of large samples of pions, kaons, and protons. In addition, at the inclusive level, identified kaons allow invariant mass studies, in particular detection of open heavy-flavoured states and vector-meson resonances such as the ϕ mesons, on which this thesis is about [17].

The detector covers a cylindrical surface of polar acceptance $|\theta - 90°| < 45°$. It has a modular structure corresponding to 18 sectors in φ and to 5 segments in z direction. The

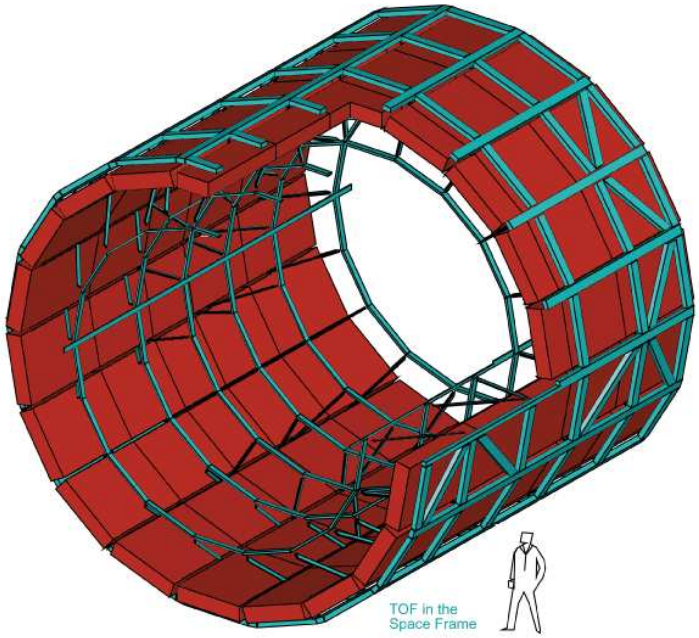

Figure 2.7: TOF detector design.

whole device is inscribed in a cylindrical shell with an internal radius of 370cm and an external one of 399cm. The basic unit of the TOF system is a 10-gap double-stack MRPC[1] strip 122 cm long and 13 cm wide, the key aspects of these chambers is that the electric field is high and uniform over the full sensitive gaseous volume of the detector. Any ionization produced by a traversing charged particle immediately starts a gas avalanche process which generates the observed signals on the pick-up electrodes. Unlike other types of gaseous detectors, there is no drift time associated with the movement of the electrons to a region of high electric field. Thus the time jitter of these devices is caused by the fluctuations in the growth of the avalanche [26].

[1]Multi-gap Resistive-Plate Chamber

Chapter 3

Particle Identification in ALICE

3.1 AliRoot framework

The ALICE offline framework, AliRoot[25], is shown schematically in figure 3.1. Its implementation is based on Object-Oriented techniques for programming and, as a supporting framework, on the ROOT system, complemented by AliEn system which gives access to the computing Grid. These fundamental technical choices result in one single framework, entirely written in C++.

The AliRoot framework is used for simulation, alignment, calibration, reconstruction, visualization and analysis of the experimental data. AliRoot has been in continuous development since 1998. In the figure 3.1 the kinematics tree containing, for example, the physics processes at the parton level and the results of the fragmentation(primary particles) is created by event generators. The data produced by the event generators contain full information about the generated particles: type, momentum, charge, and mother-daughter relationship. The hits (energy deposition at a given point and time) are stored for each detector. The information is complemented by the so called *track references* corresponding to the location where the particles are crossing user defined reference planes. The hits are converted into digits taking into account the detector and associated electronics response function. Finally, the digits are stored in the specific hardware format of each detector as raw data. At this point the reconstruction chain is activated.

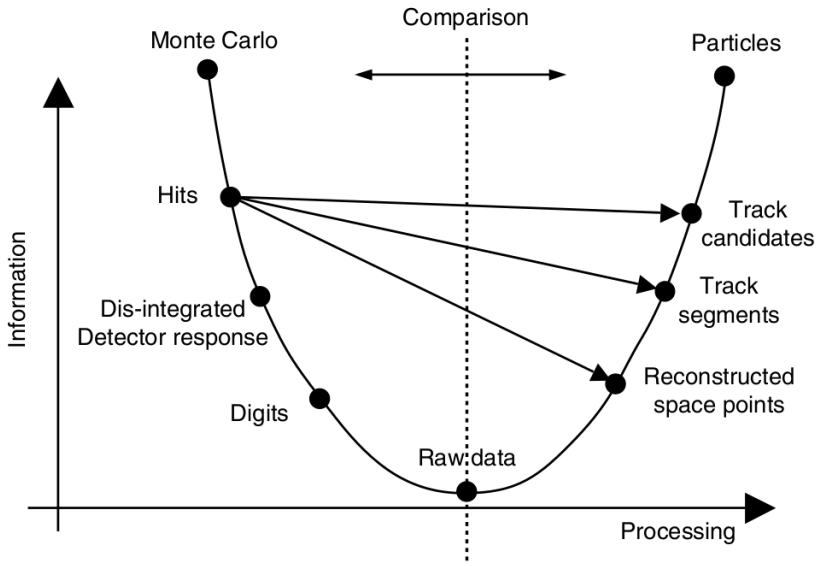

Figure 3.1: Data processing framework

3.2 TPC PID

From the TPC, the number of clusters assigned n_{cl} to each track the energy loss (dE/dx) information can be extracted, having in each cluster a total charge Q_{tot}, representing the sum over the pads in the row. In the measured energy loss there is a tail towards higher energy losses, this leads to a problem because the average energy loss would not be a good estimator for the mean energy loss as it would be for a Gaussian distribution. Therefore the truncated mean method is used to overcome this problem. It is characterized by a cut-off parameter η between 0 and 1. The truncated mean $\langle S \rangle_\eta$ is then defined as the average over the m=ηn lowest values among the n_{cl} samples:

$$\langle S \rangle_\eta = \frac{1}{m} \sum_{i=0}^{m} Q_i \tag{3.1}$$

where i = 0,...,n and $Q_{i-1} \leq Q_i$ for all i. If one simulates with the Monte Carlo method based on typical ionization distributions the measurement of many tracks in order to determine an optimal value for η, one finds a value between 0.35 and 0.75. For the ALICE TPC this value is currently set to $\eta = 0.5$.

The signals in the TPC can be identified as a certain type of particles (electrons, pions, kaons, protons, etc) by the Bethe-Bloch formula. This formula can describe the energy loss

curve of a particle with mass m traversing certain medium, this parametrization has been previously used by the ALEPH experiment[24] as follows:

$$f(\beta\gamma) = \frac{P_1}{\beta^{P_4}}(P_2 - \beta^{P_4} - ln(P_3 + \frac{1}{(\beta\gamma)^{P_5}})) \tag{3.2}$$

where the parameters P_i depend on the data sample being analysed. The figure 3.2 shows the TPC energy loss as a function of momentum as well as the Bethe-Bloch parametrization curves for each type of particle.

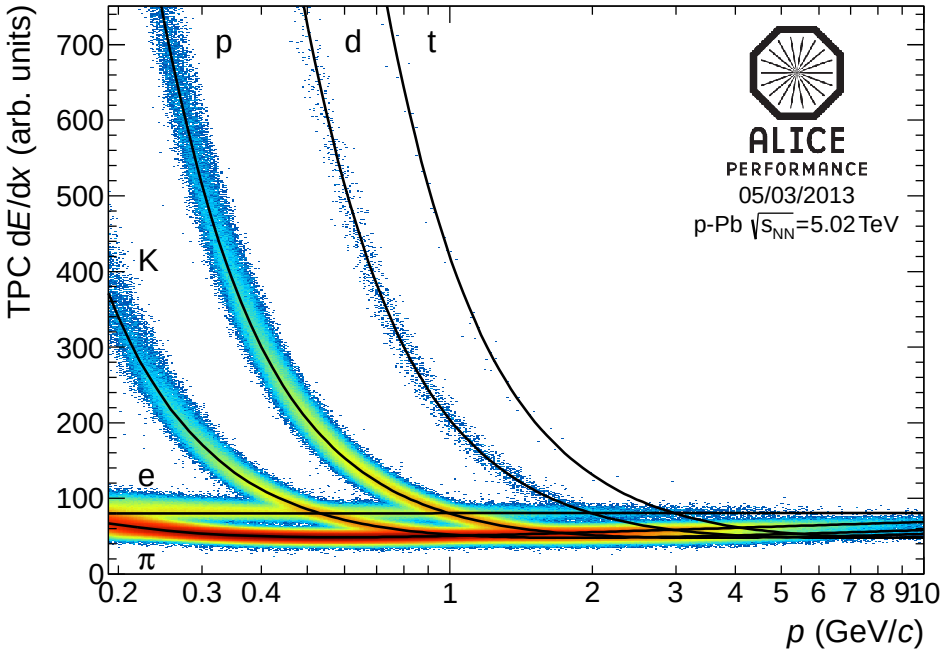

Figure 3.2: dE/dx-spectra from TPC detector together with a Bethe-Bloch curve for each particle. Signals coming from p-Pb collisions.

The particles are identified by selecting certain range ($2\sigma, 3\sigma$, etc) from the Bethe-Bloch curve parametrized to each type of particle.

3.3 TOF PID

The TOF detector, differently from TPC, does not identify particles by the energy loss. Instead it uses the time the particle travels from the primary vertex to one of the TOF sensitive pads. In ALICE, the TOF particle identification is based on the comparison between

the time-of-flight measured by TOF ($t_{\rm TOF}$) and the expected time ($t_{\rm exp,i}$)). The latest is calculated in terms of the momentum, length L and mass hypothesis i of each type of particle as follows:

$$(t_{\rm exp,i}) = \sum_{\rm k} \Delta t_{i,{\rm k}} = \sum_{\rm k} \frac{\sqrt{p_{\rm k}^2 + m_i^2}}{p_{\rm k}} \Delta l_{\rm k} \tag{3.3}$$

In order to take into account the energy loss and the consequent variation in the track momentum, ($t_{\rm exp,i}$)) is calculated as the sum over k of the small time increments $\Delta t_{i,{\rm k}}$; the time a particle of mass m_i and momentum $p_{\rm k}$ takes to travel along each propagation step k (of $\Delta l_{\rm k}$ length) during the track reconstruction procedure. To perform TOF particle identification it is necessary to define $t_{\rm TOF} - t0 - t_{\rm exp,i}$, where t0 is subtracted. The resolution for the mass hypothesis i ($\sigma_{\rm PID,i}$), is the combination of the TOF detector time resolution ($\sigma_{\rm TOF}$), the time-zero resolution ($\sigma_{\rm t0}$) and the tracking resolution ($\sigma_{t_{\rm exp}}$), and the expression is given as follows:

$$\sigma_{\rm PID,i} = \sqrt{\sigma_{\rm TOF}^2 + \sigma_{\rm t0}^2 + \sigma_{t_{\rm exp}}^2} \tag{3.4}$$

where $\sigma_{t_{\rm exp}}$ is defined as:

$$\sigma_{t_{\rm exp}}^2 = \left(\frac{\Delta p \cdot t_{\rm exp,i}}{1 + \frac{p^2}{m_i^2}} \right)^2 \tag{3.5}$$

and assuming that the resolution on the length of the track is negligible with respect to the one on the momentum and Δp.

The PID separation relies on the difference between the observed time-of-flight ($t_{TOF} - t0$), and the expected time $t_{exp,i}$ for all the particles types (π, K, p). The particle separation is in terms of $n\sigma$ as:

$$n\sigma_i = \frac{t_{\rm TOF} - t0 - t_{\rm exp,i}}{\sigma_{\rm PID,i}} \tag{3.6}$$

where $\sigma_{\rm PID,i}$ is shown in eq. 3.4. The specific $n\sigma$ cuts for kaons are explained in the next chapter; where the analysis details are discussed.

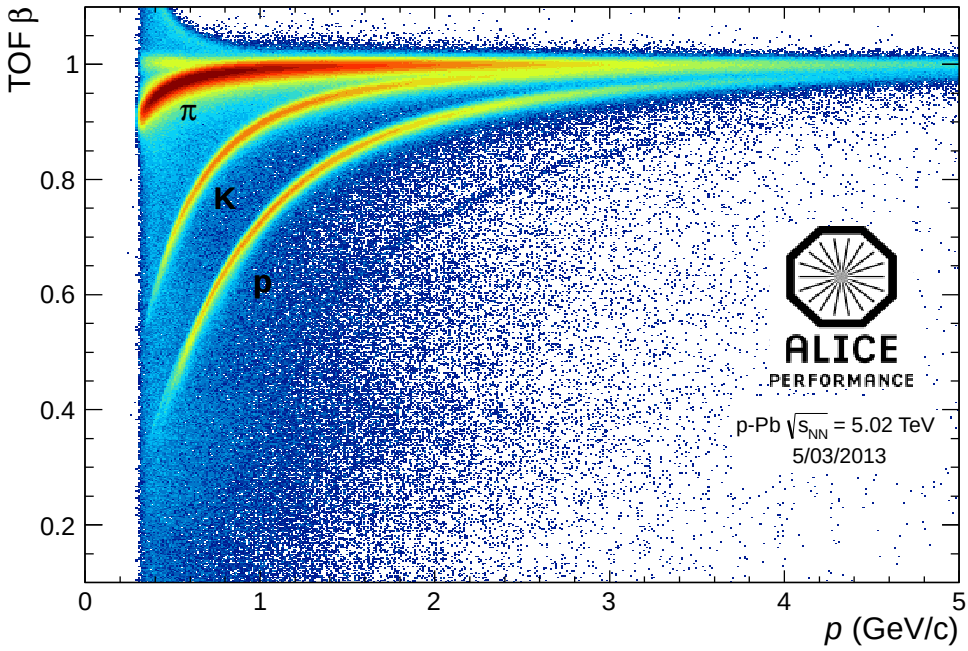

Figure 3.3: TOF signal as a function of momentum. The clear bands correspond to each type of particle.

Chapter 4

$\phi(1020)$ Analysis Results

4.1 Event and Track Selection

In this section the characteristics of the event selection and the corresponding tracks used to measure the $\phi(1020)$ mesons will be described in detail.

4.1.1 Event Selection

The collision system p-Pb at $\sqrt{s_{NN}} = 5.02$ TeV collected by ALICE in the beginning of 2013, is analyzed in the present work. Because of the 2-in-1 magnet design of the LHC[28], the energy of the two beams cannot be adjusted independently, leading this to a different energies per beam due to the different Z/A. The nucleon-nucleon center-of-mass system, therefore, is moved in the laboratory frame with a rapidity of $y_N = -0.465$ in the proton beam direction.

The events selected are those that passed some standard cuts. Events are accepted if they have a primary vertex, reconstructed in the SPD, whose z coordinate is within ± 10 cm from the interaction point. The multiplicity classes in the events are selected in terms of percentiles of the raw multiplicity estimator, being the V0A (in Pb direction) the detector that provides the multiplicity information. The cuts applied to the events are the following:

- Physics Selection Task, which selects events according to the ALICE triggers definitions. In this work the trigger used was kINT7.
- Events required to have a reconstructed primary vertex.

- Events with vertex-z cut of $\mid v_z \mid < 10$ cm.
- Multiplicity ranges (V0A): 0-5%,5-10%,10-20%,20-40%,40-60%, 60-80% and 0-100% .

After the trigger and vertex selection described before, the total number of Minimum Bias events analyzed is 9.4×10^7. In the figure 4.1 the multiplicity distribution of the accepted events, divided in ranges of multiplicity percentage, is shown.

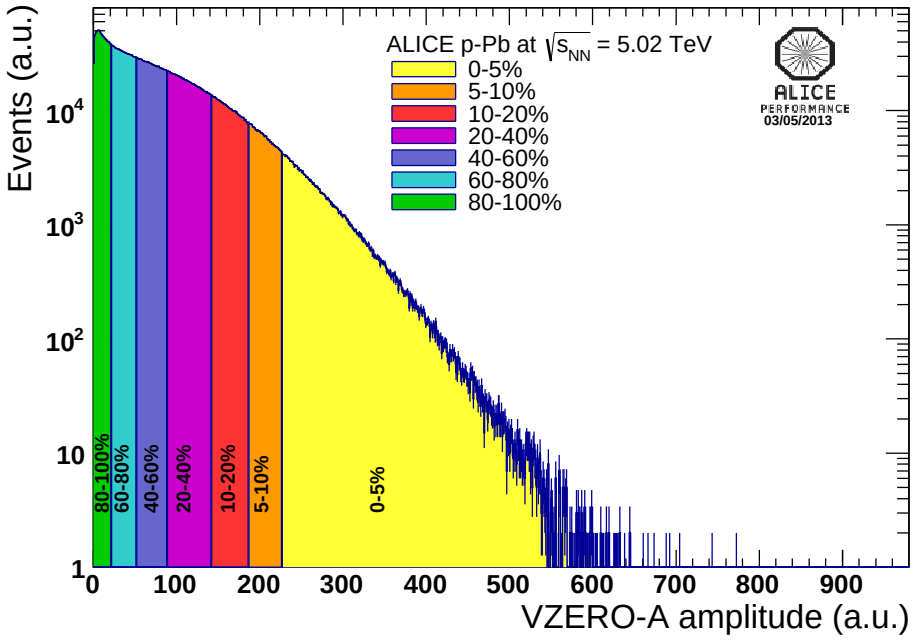

Figure 4.1: V0A particles multiplicity in terms of percentile ranges.

4.1.2 Track selection

The primary particles are those produced in the collision including weak and electromagnetic decays products, but excluding products from strange weak decays and particles from secondary interactions. In ALICE we have a set of track cuts that are optimized to select the primary particles, this set is known within the Collaboration as the *2011 Standard Track Cuts* and they are summarized in the list below.

- Tracks are required to have at least 70 crossed rows in the TPC, and a χ^2 of the momentum fit smaller than 4 per cluster.

- The Distance-of-Closest Approach (DCA) in the Z direction to the reconstructed event vertex is required to be less than 2 cm and in the XY plane less than $0.0105+0.0350/p_{\mathrm{T}}^{1.1}$ cm.
- At least two clusters in the ITS must be associated to the track.
- χ^2 per ITS cluster less than 36.
- TPC and ITS refit.
- Pions and kaons daughter rejection.

The ϕ mesons are identified via two charged kaons ($\phi \rightarrow K^-K^+$), which is the most probable decay channel (branching ratio of 0.489± 0.005). Also, for a pair of kaons to be considered as a ϕ candidate, its rapidity was asked to be within the range $0 < \mathrm{y}_{cms} < 0.5$ [27].

4.2 $\phi(1020)$ Meson Identification

4.2.1 Kaon identification

After applying the track selection cuts mentioned in the previous section, the kaons are identified through their time of flight signal in the TOF (Time of Flight) detector and their energy loss in the TPC (Time Projection Channel). The advantage of using both detector combined procedure is that TPC can provide track information at low transverse momentum $p_{\mathrm{T}} < 1.0$ GeV/c and TOF contribute to reduce the background at high transverse momentum $p_{\mathrm{T}} > 5.0$. Whenever a track has TOF information it is taken in the analysis and when this is not the case the TPC information is used. Two different cuts in $N\sigma$ for kaons are used, $|n\sigma_{K,TPCTOF}| < 3$ and $|n\sigma_{K,TPCTOF}| < 4$. The figure 4.2 shows the PID response $(n - \sigma)$ as a function of p_{T} for TOF and TPC detectors, taking the kaon hypothesis.

4.2.2 Invariant Mass

Having the kaons identified by the n-sigma method described before, then the ϕ invariant mass has to be calculated in function of energy and momentum from each kaon daugh-

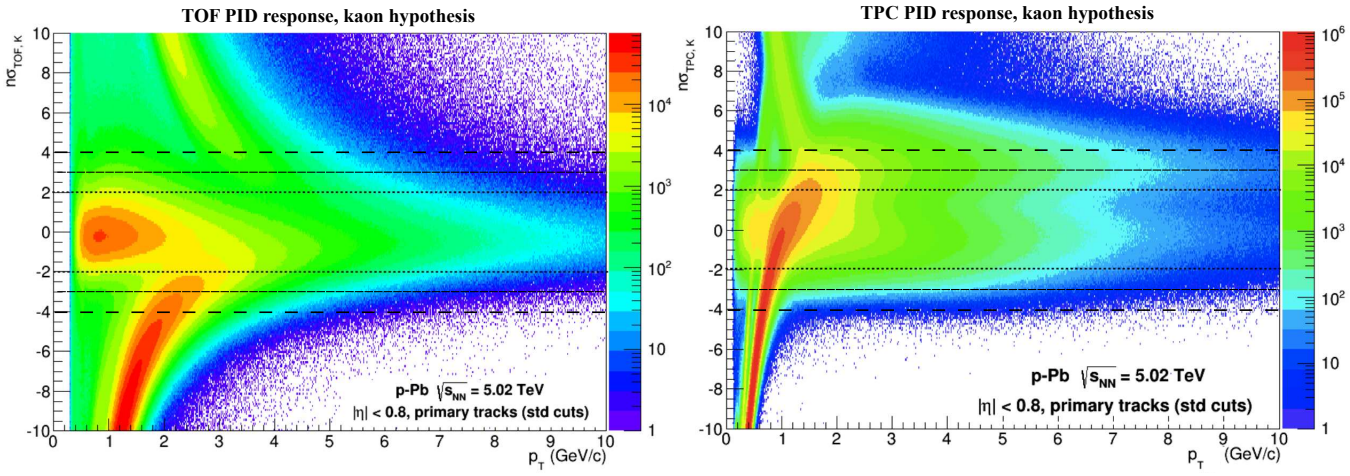

Figure 4.2: Left: TOF PID response for the kaon hypothesis. Right: TPC PID response for the kaon hypothesis. Dashed lines correspond to 2σ, 3σ and 4σ particle selection limits.

ter. If the first and second kaon daughters are denoted by the subscript numbers 1 and 2 respectively, then the invariant mass equation is given as follows:

$$M_{inv}^2 = (p_1^2 + p_2^2) = (E_1 + E_2)^2 - (\mathbf{p_1} + \mathbf{p_2})^{\mathbf{2}} \tag{4.1}$$

The figures 4.3 and 4.4 show the ϕ invariant mass (eq. 4.1) distribution in all the p_{T} ranges analyzed. A prominent peak is located at $M_{k^+k^-} \approx 1.02$ GeV/c^2, corresponding to the ϕ mass range. From the plots a large background below the signal is notorious and needs to be subtracted in order to extract the ϕ meson yield.

4.2.3 Combinatorial Background Subtraction

Depending on the underlying physics and on the event multiplicity, the background originates from uncorrelated particles and/or from correlated particles i.e. of common origin. In principle if one choses appropriate functions, the signal can be extracted by fitting the signal+background distributions, but this technique, however, does not work if signal and background have a similar shape. Then, the only way to overcome this problem is to estimate independently the background distribution and to subtract it from the signal+background spectrum. Two methods are used to estimate the combinatorial background, the Event Mixing and Like Charge. In this analysis the default method is Event Mixing, being Like Charge used only as a cross check because it does not have a good reproduction of the

background shape.

1. **Event Mixing (default choice):** Invariant-mass distribution are calculated for pairs of oppositely charged kaons from different events. Each event analyzed is mixed with 5 other events in which for a pair of events, the difference in vertex-z is required to be less than 1 cm and the multiplicity percentile difference is required to be less than 10%.

2. **Like Charge:** Invariant-mass distribution are calculated using pairs of kaons with the same charge from the same event. In each invariant mass bin, the value of the like-charge background is $2\sqrt{N^{--}N^{++}}$, where $N^{--}(N^{++})$ is the number of $K^-K^-(K^+K^+)$ pairs in the bin.

The figures 4.3 and 4.4 show the invariant mass distributions of the unlike-charge and mixed events in all p_{T} bins analyzed. Where the mixed event background is normalized in such a way that it has the same integral as the unlike-charge distribution in a given invariant mass range. The normalization region chosen as default is: $1.04 < m < 1.06$ GeV/c^2.

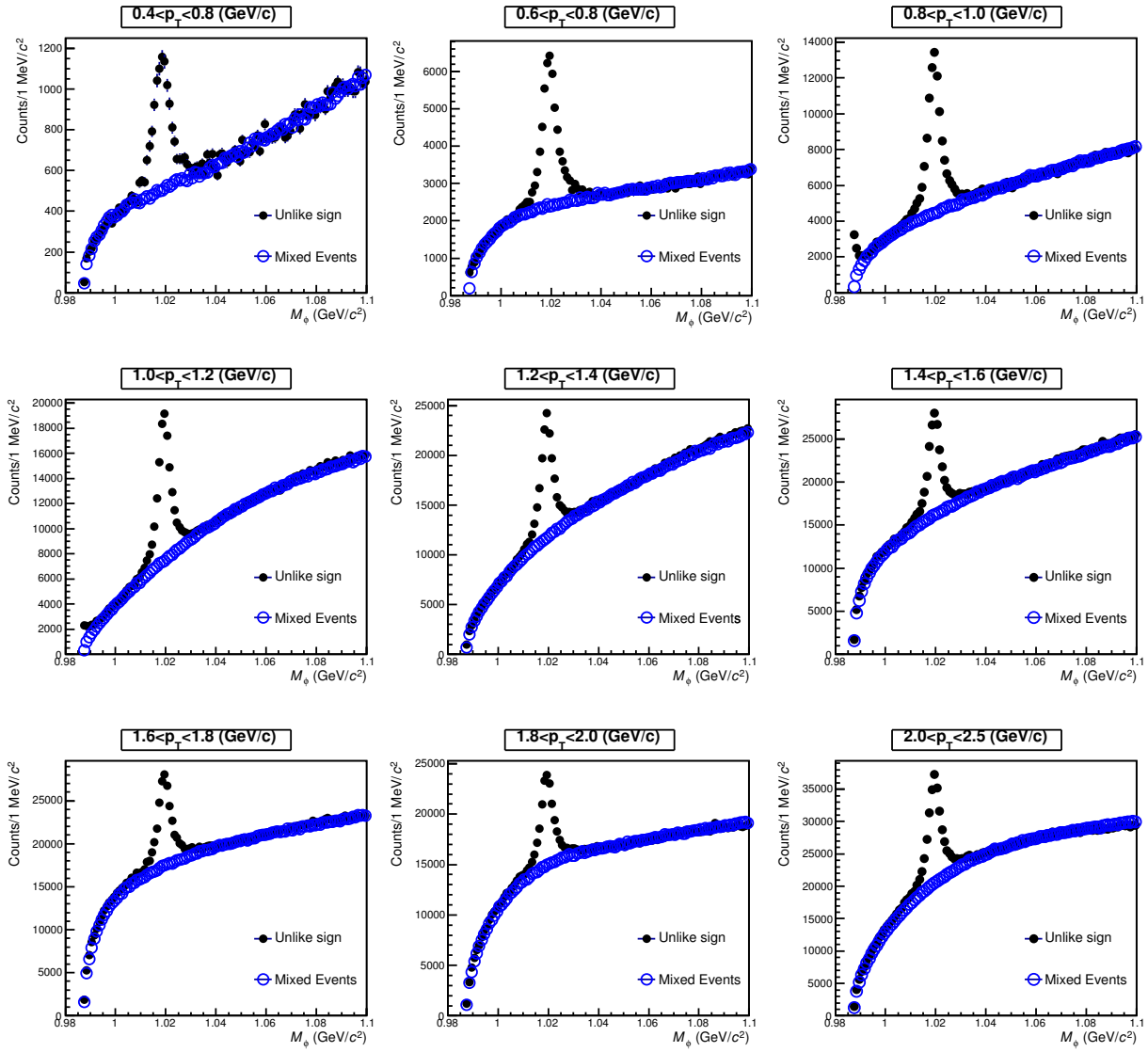

Figure 4.3: K^+K^- Invariant mass distributions in several p_{T} ranges are shown as black points and the combinatorial background(event mixing) are blue points.

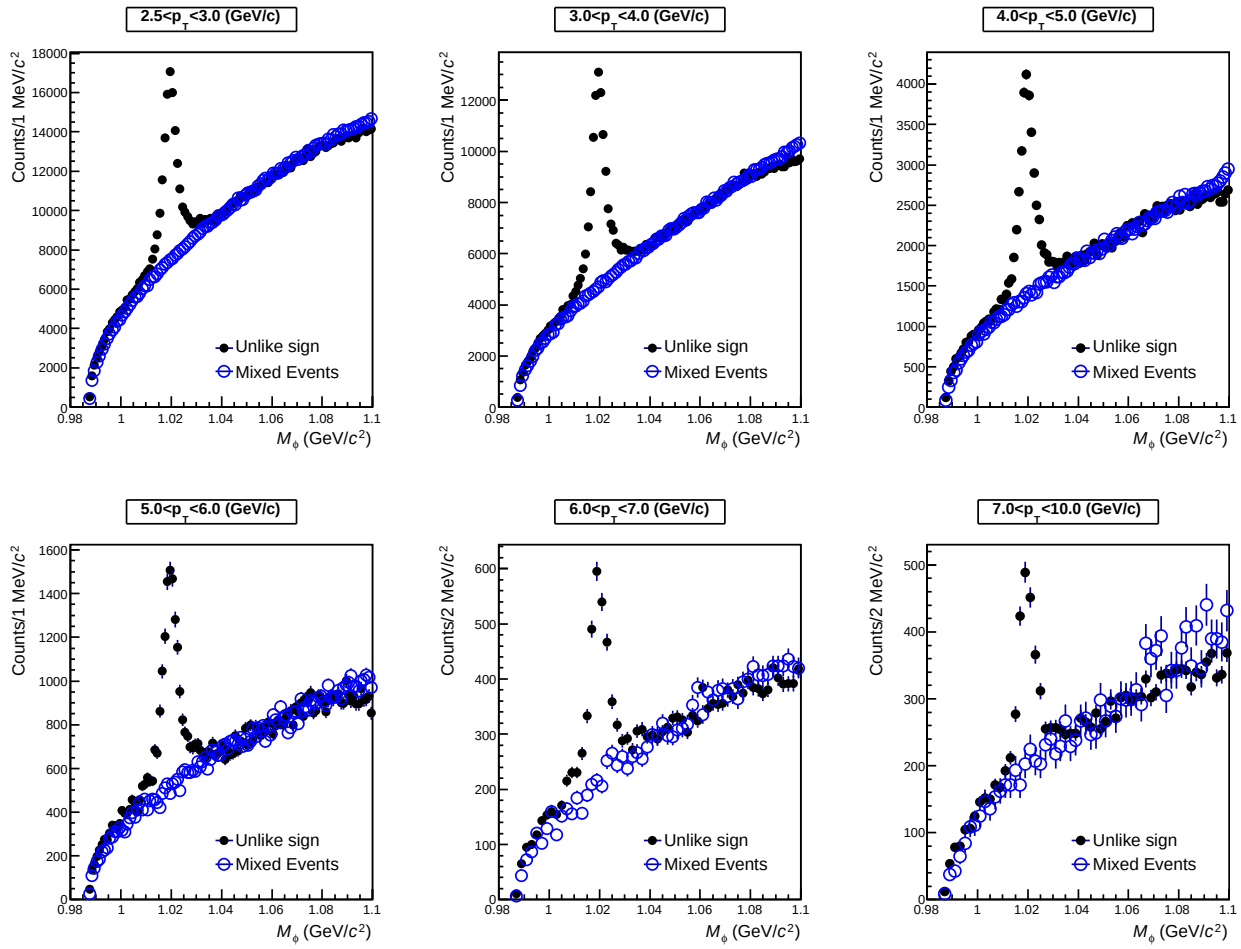

Figure 4.4: K^+K^- Invariant mass distributions for high p_{T} values are shown as black points and the combinatorial background(event mixing) are blue points.

4.2.4 Peak and Residual Background Fits

After the combinatorial background is subtracted, by the Mixed Event method, some residual background might be still present and has to be subtracted. It is estimated by fitting the invariant-mass distribution (combinatorial background subtracted) with a polynomial function. Two functions are used to estimate the residual background: linear and quadratic functions, the last one being the default choice. After the background subtractions the peak is fitted by two basic functions: the relativistic Breit-Wigner function and a Voigtian function.

- **Breit-Wigner:** The relativistic Breit-Wigner distribution (after the 1936 nuclear resonance formula[20] of Gregory Breit and Eugene Wigner) is a continuous probability distribution with the following probability density function,

$$f(E) = \frac{k}{(E^2 - M^2)^2 + M^2\Gamma^2}, \tag{4.2}$$

where k is a constant of proportionality, equal to

$$k = \frac{2\sqrt{2}M\Gamma\gamma}{\pi\sqrt{M^2 + \gamma}} \text{ with } \gamma = \sqrt{M^2(M^2 + \Gamma^2)}. \tag{4.3}$$

It is widely used to model resonances in high energy physics. In this case, E is the center of mass energy that produces the resonance, M is the mass of the resonance, and Γ is the resonance width(or decay width), related to its mean lifetime according to $\tau = 1/\Gamma$. For values of E off the maximum at M such that $|E^2 - M^2| = M\Gamma$, (hence $|E - M| = \Gamma/2$ for $M \gg \Gamma$), the distribution f has attenuated to half its maximum value, which justifies the name for Γ sharpens infinitely to $2M\delta(E^2 - M^2)$. The form of the relativistic Breit-Wigner distribution arises from the propagator of an unstable particle, which has a denominator of the form $p^2 - M^2 + iM\Gamma$. The propagator in its rest frame then is proportional to the quantum-mechanical amplitude for the decay utilized to reconstruct that resonance,

$$\frac{\sqrt{k}}{(E^2 - M^2) + iM\Gamma} \tag{4.4}$$

The resulting probability distribution is proportional to the absolute square of the amplitude, so then the above relativistic Breit-Wigner distribution for the probability

density function. This function was only used just as a cross-check for the ϕ yield, so it was not included in the systematic analysis.

- **Voigtian:** The Voigt profile (named after Woldemar Voigt) is a line profile resulting from the convolution of two broadening mechanisms, one of which alone would produce a Gaussian profile, and the other would produce a Lorentzian profile[21]. The Lorentzian describe the ideal resonance signal and the Gaussian accounts for the detector resolution. It is implemented using the following function:

$$\frac{\mathrm{d}N}{\mathrm{d}m_{KK}} = \frac{A\Gamma}{(2\pi)^{3/2}\sigma} \times \int_{-\infty}^{\infty} \exp\left[-\frac{(m_{KK}-m')^2}{2\sigma^2}\right] \frac{1}{(m'-M_0)^2+\Gamma_0^2/4}\mathrm{d}m' \tag{4.5}$$

  where σ is the mass resolution parameter which is p_{T}-dependent and is fixed to the value found from simulated data, this procedure is described in Appendix .0.1.

Both, the peak and residual background, are fitted in the invariant mass region: $0.99 < M_{\phi} < 1.09$ GeV/c^2. The resolution is allowed to vary freely and the width parameter (Γ) is fixed to the PDG value 4.26 MeV/c^2. In the figures 4.5 and 4.6 is shown the combinatorial background subtracted invariant mass, along with the Voigtian and residual background fits, for several p_{T} ranges of the ϕ meson. Then after subtracting the combinatorial background and after fitting the residual background the raw yield is determined as:

$$N^{raw} = N^{counts} - Integral^{pol2},$$

where N^{counts} is the total number of counts in the mass region of $1.01 < m < 1.03$ GeV/c^2 in the combinatorial background subtracted histogram. And $Integral^{pol2}$ is the integral over the same mass region of the second order polynomial function that is fitted to the residual background. Absolute statistical uncertainty for the raw yield is determined as $\sqrt{A^2 + Integral^2_{stat}}$, where $A = \sqrt{\sum_{n=i} \delta_n^2}$ and δ_n is the statistical error of the n-th bin after mixed background subtraction. And $Integral^2_{stat}$ is the statistical error of the polynomial integral.

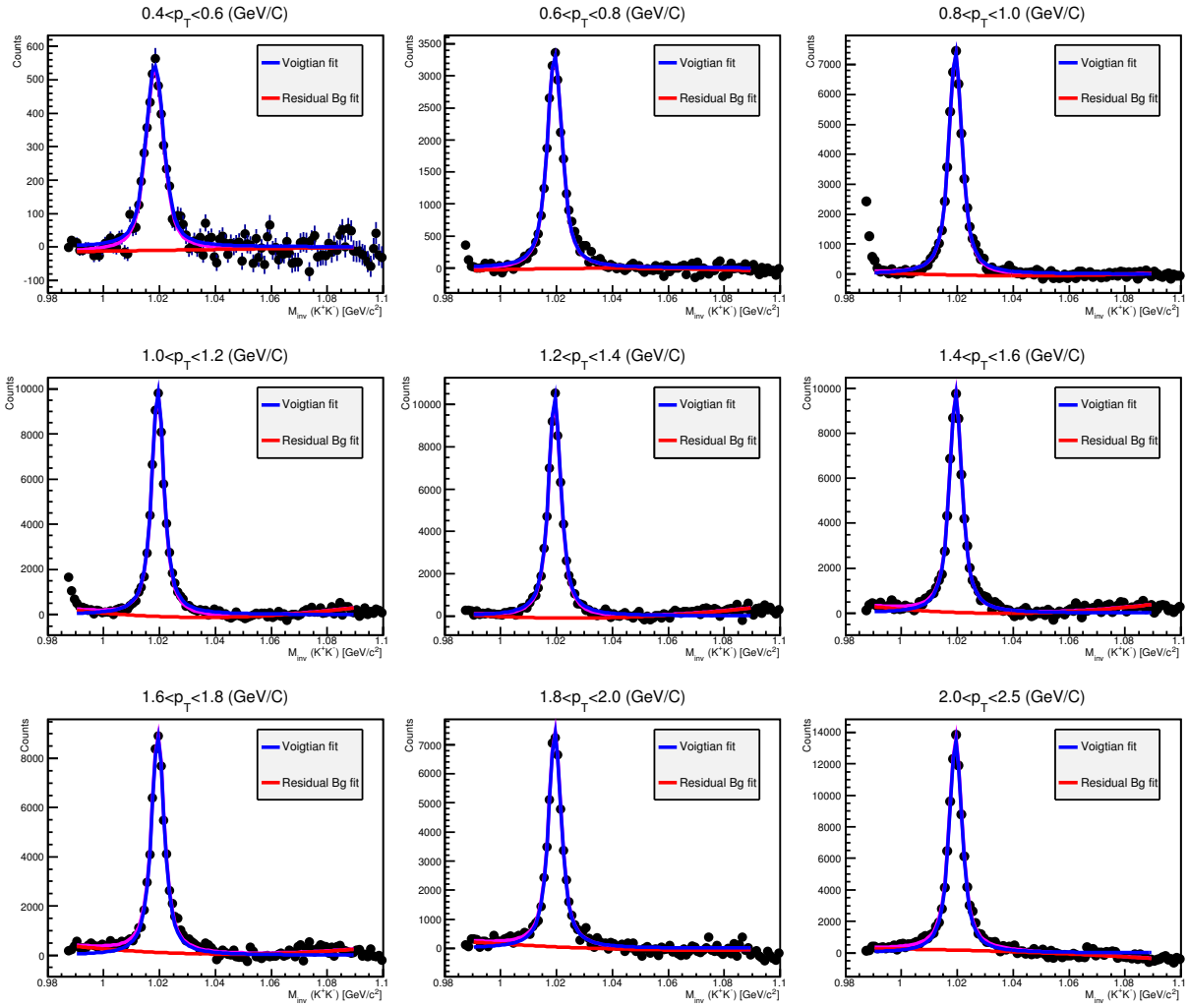

Figure 4.5: Invariant mass distribution after the mixed events background subtraction using the information from TPC and TOF combined. Results correspond to 0-100% multiplicity bin, magenta line is the total fit (ResidualBg+Voigt).

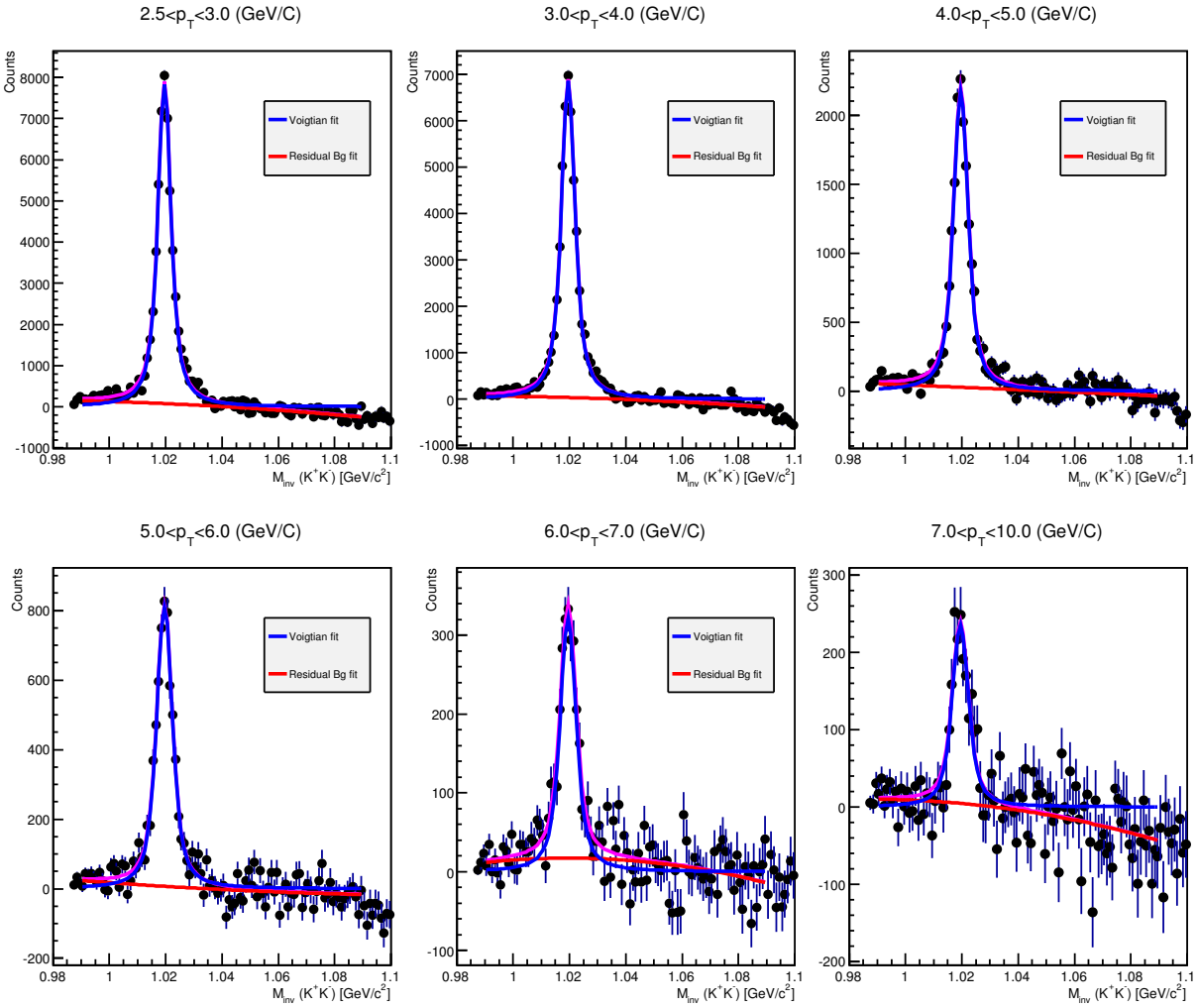

Figure 4.6: Invariant mass distribution after the mixed events background subtraction using the information from TPC and TOF combined. Results correspond to 0-100% multiplicity bin, magenta line is the total fit (ResidualBg+Voigt).

4.2.5 Raw Yield Calculation

The ϕ yield is calculated using two methods. In the **default method**, the yield is extracted by integrating the invariant mass histogram over the region $1.01 < m < 1.03$ GeV/c^2 and subtracting the integral of the residual background that is fitted in the same region, as described previously.

The second method consist in integrating the fit function which is a Voigtian function with fixed width Γ =4.26 MeV, value obtained from the PDG. The function is integrated in the mass region $2M(K^{\pm}) < m < \infty$, the mass region below 2M($K^{\pm}$) = 0.987334 GeV/c^2 is kinematically forbidden[30]. Therefore, the yield is given by

$$Yield = \int_{2M(K^{\pm})}^{\infty} peak(m)\mathrm{d}m \tag{4.6}$$

4.2.6 Peak Correction Factor

Since the default method used in this analysis is integrating the invariant-mass distribution over the range $1.01 < m < 1.03$ GeV/c^2 to get the ϕ yield, a correction factor is necessary to account for the portion of the yield that lies outside the range of integration. This correction is the peak factor, and it is calculated as follows:

$$\epsilon_{PC} = \frac{\int_{1.01}^{1.03} fit(\mathrm{m})\mathrm{dm}}{\int_{2M(K^{\pm})}^{\infty} fit(\mathrm{m})\mathrm{dm}}. \tag{4.7}$$

Here, the numerator in ϵ_{PC} is the integral in the default range (1.01¡m¡1.03 GeV/c^2) of the fit to the background-subtracted invariant mass distribution. The denominator is the integral of the same function over a wider range, starting from $2M(K^{\pm})$ = 0.9873 GeV/c^2 up to infinity. The peak correction (ϵ_{PC}) is applied only when the default method (integrating the histogram) is used to obtain the yield. In the case when the yield is extracted by integrating the peak fit function, this correction is not applied. The figure 4.7 shows an example of the peak correction factor in the $0-100\%$ multiplicity bin.

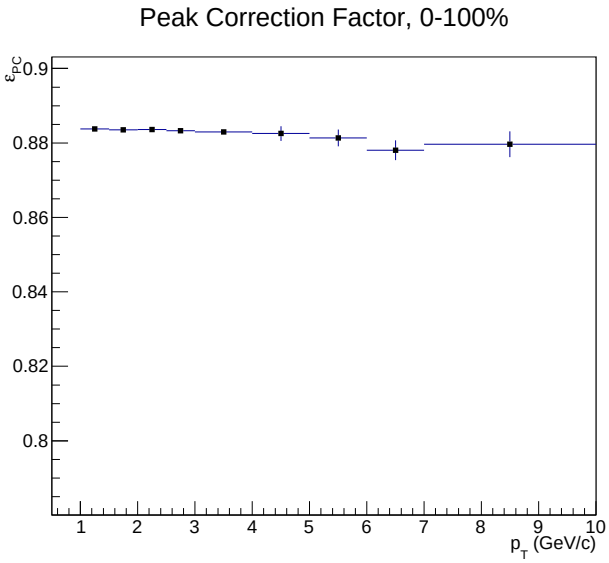

Figure 4.7: Peak correction factor for the default analysis parameters in the multiplicity bin $0-100\%$

4.3 Monte Carlo simulations

A simulation data set is analyzed in order to get information, needed to complete the real data analysis, such as: ϕ reconstruction efficiency$\times$ acceptance, the ϕ mass resolution (used as a Voigtian parameter in the real data fits), mass and width.

The simulation data set analyzed is the production (ESDs): LHC13b2_efix_p1, LHC13b2_efix_p2, LHC13b2_efix_p3, LHC13b2_efix_p4, produced by the DPMJET event generator, the particle interaction with the ALICE detectors are simulated using GEANT3. After all the event selection cuts and track quality cuts, which are the same used in real data (see 4.1), the number of selected events is 99 million.

4.3.1 Reconstruction Efficiency

In the context of this section the 'generated' particles are referred as the ones produced by the event generator(DPMJET) for p-Pb collisions without any detector effects. The 'reconstructed' tracks are those that passed through the reconstruction algorithms, the selected reconstructed particles are primary kaons that passed the same track cuts as in data (see 4.1) including the PID cuts in the detectors. A reconstructed ϕ meson is a ϕ for which both daughter tracks (K^+, K^-) have been reconstructed by the algorithms. The total ϕ

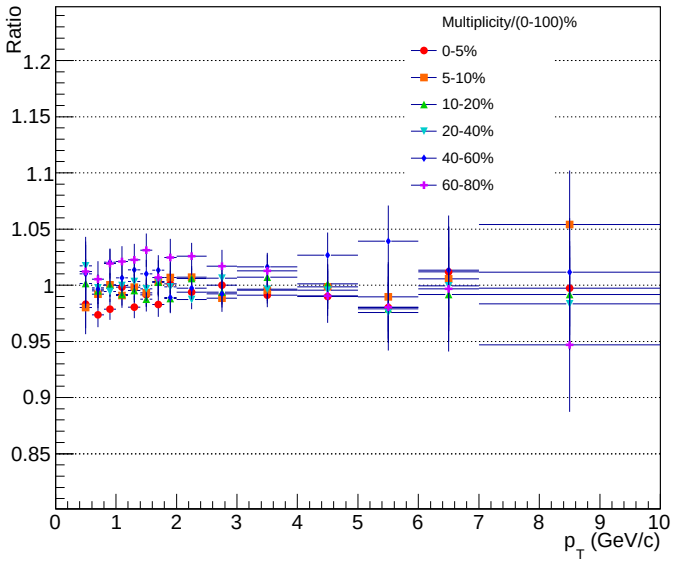

Figure 4.8: Ratios of the efficiency as a function of multiplicity over the Minimum Bias efficiency (0-100)%.

reconstruction efficiency is given by:

$$\epsilon_{rec} = \frac{\phi_{reconstructed,TPC-TOF}}{\phi_{generated}}, \quad \text{where} \tag{4.8}$$

- **Generated ϕ:** Are the generated ϕ mesons from the events that fulfil the requirements of the Event Selection Cuts, described in section 4.1. The ϕ particles are asked to be within a rapidity region $0 < y_{cms} < 0.5$.

- **Reconstructed ϕ:** The number of ϕ mesons within a rapidity region $0 < y_{cms} < 0.5$ for which both kaons decay daughters are reconstructed and passed the track selection cuts and either TPC or TOF PID nσ-cuts.

In the figure 4.9 ϵ_{rec} is shown as a function of p_T, for each nσ cut applied, where a strong variation in the low part of the transverse momentum is observed but no strong dependence on multiplicity. This can be seen by doing ratio of the multiplicity dependent efficiency over the minimum bias(0-100%) one, the figure 4.8 shows this ratio from which we see clear that the variations are less than 5%.

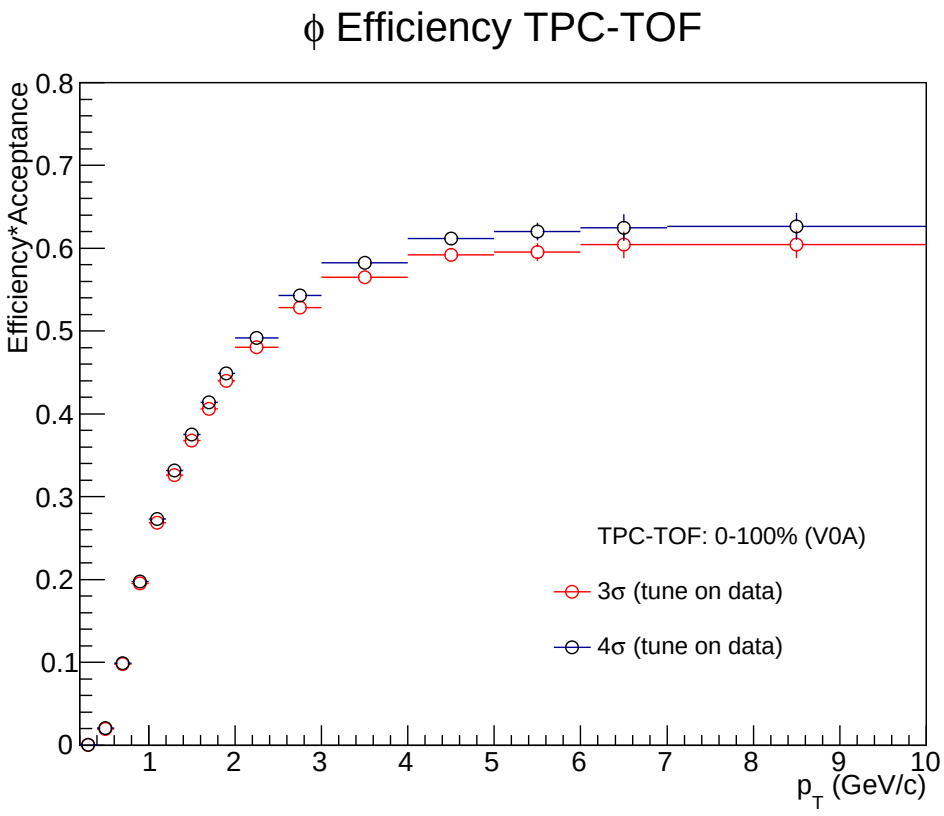

Figure 4.9: Efficiency used to correct the TPC-TOF data, 3σ and 4σ are shown.

Chapter 5

$\phi(1020)$ Spectra And Systematic Analysis

5.1 $\phi(1020)$ Invariant Spectra

After obtaining the ϕ uncorrected yield in each multiplicity and p_{T} bin, some factors and corrections need to be applied to the Raw Yield these corrections are summarized in the equations 5.1 and 5.2:

$$\frac{d^2\mathrm{N}_{raw}}{\mathrm{d}p_{\mathrm{T}}\mathrm{d}y} = \frac{Raw \quad Yield}{\mathrm{N}_{evt} \times BR \times \mathrm{d}p_{\mathrm{T}}\mathrm{d}y} \tag{5.1}$$

where Raw Yield is the integral of the entries in the ϕ invariant mass distribution (see 4.2.5), N_{evt} is the number of analyzed events in each multiplicity range, $BR = 0.489$ is the $\phi \rightarrow \mathrm{K}^+\mathrm{K}^-$ branching ratio, $\mathrm{d}p_{\mathrm{T}}$ is the width of the p_{T} bin analyzed and dy = 0.5 is the rapidity bin.

The corrections to the ϕ spectra are:

- ϵ_{rec} : Reconstruction efficiency $\times$ acceptance for the TPC-TOF detector combination, in this efficiency is included the nσ cut (see Section 4.3.1).
- ϵ_{PC} : Peak correction factor(see Section 4.2.6).
- ϵ_{trig} : Correction that accounts for trigger and vertex efficiency for NSD collisions, it has a value of $97.8 \pm 1\%$ for Minimum Bias measurements.

Taking into account the normalization and the corrections listed above, the corrected ϕ meson spectra is calculated as follows:

$$\frac{d^2N}{\mathrm{d}p_\mathrm{T}\mathrm{d}y} = \frac{\mathrm{d}^2N_{raw}}{\mathrm{d}p_\mathrm{T}\mathrm{d}y} \cdot \frac{\epsilon_{trig}}{\epsilon_{rec}\epsilon_{PC}} \tag{5.2}$$

The figure 5.1 shows the fully corrected ϕ spectra (eq. 5.2) as a function of p_T for all the multiplicity ranges analyzed.

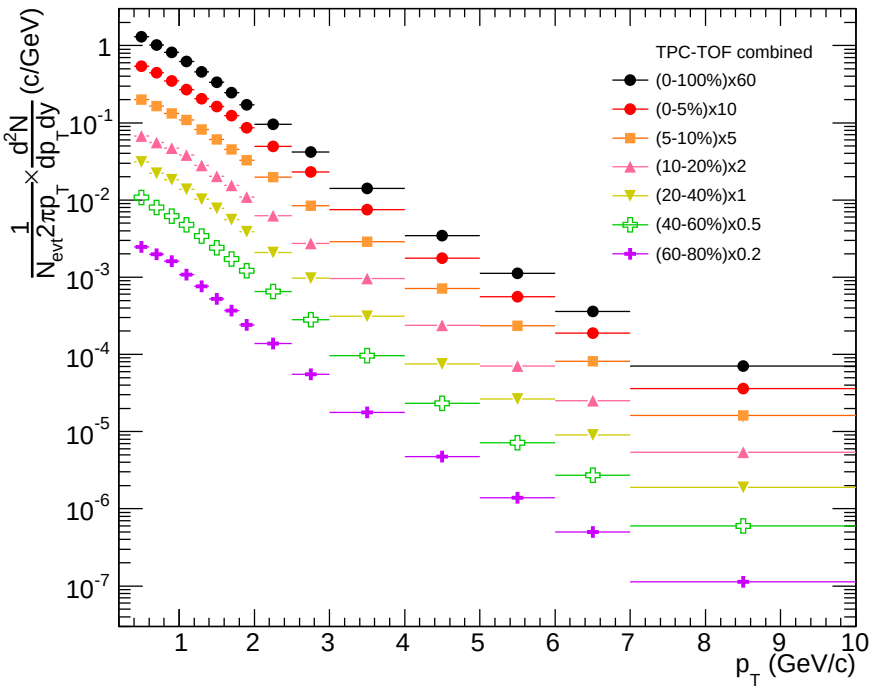

Figure 5.1: Fully corrected ϕ Spectra $1/2\pi p_\mathrm{T} \times (d^2N/dp_\mathrm{T}dy)$ obtained with TPC-TOF detectors information, for Minimum Bias, 0-5%, 5-10%, 10-20%, 20-40%, 40-60% and 60-80% multiplicity measurements. Only statistical errors are shown.

5.2 Mass and Width

The mass and width values are obtained from the Voigtian fit parameters for each p_T bin. For the mass case, the width parameter in the Voigtian function was fixed to the PDG value (4.26 MeV/c^2) while for the width measurement only the resolution parameter is fixed to the

σ_{voi} value (see Appendix .0.1). The figure 5.2 shows the mass as a function of p_{T}, for three measured multiplicities: central, peripheral and Minimum Bias. In the low-intermediate p_{T} the points agree within the statistical uncertainties, except for the first point, that is clearly bellow the PDG value and needs further investigations. At high p_{T} large statistical errors are present mainly due to the low statistics in the multiplicity measurements.

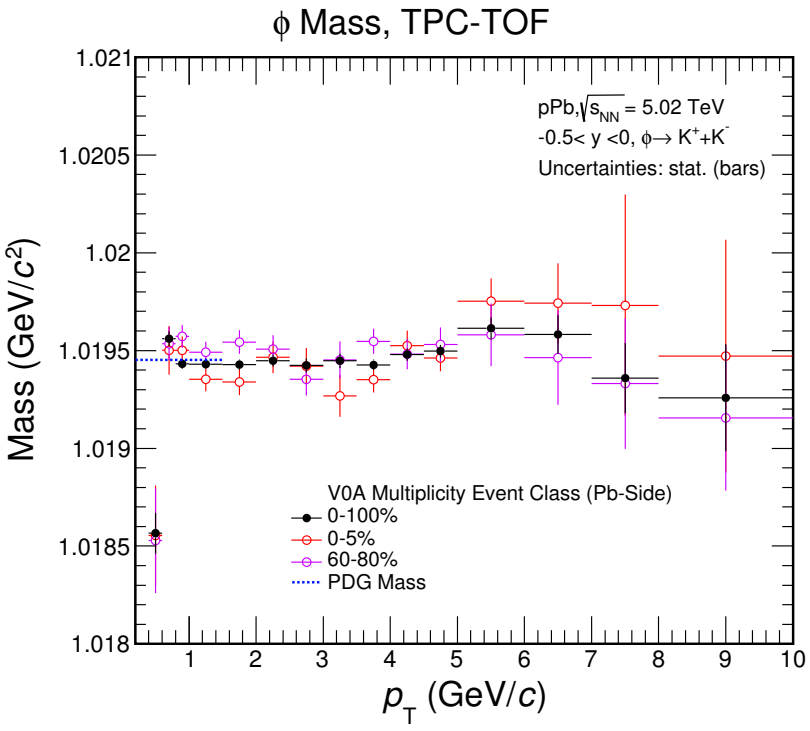

Figure 5.2: Mass of the ϕ mesons measured in Minimum bias, 0-5% and 60-80% multiplicity ranges. Only statistical uncertainties are shown.

The figure 5.3 shows the full width values in three multiplicity ranges. Some statistical fluctuations are observed in the first p_{T} bin and in high p_{T} range. Above 1 GeV/c the data points agree with the PDG width value, but below that momentum, the data point are above the PDG value. This last feature was also observed in Pb-Pb collisions[35] and in generated events based in a multiphase transport model (AMPT) at $\sqrt{s_{\mathrm{NN}}} = 39$ GeV for Au-Au collisions[36]. This deviation of the full width at low momentum can be explained from the point of view that the ϕ meson scatter before their decay into kaons inside the medium, affecting the full width as well as the mass of the resonance particle.

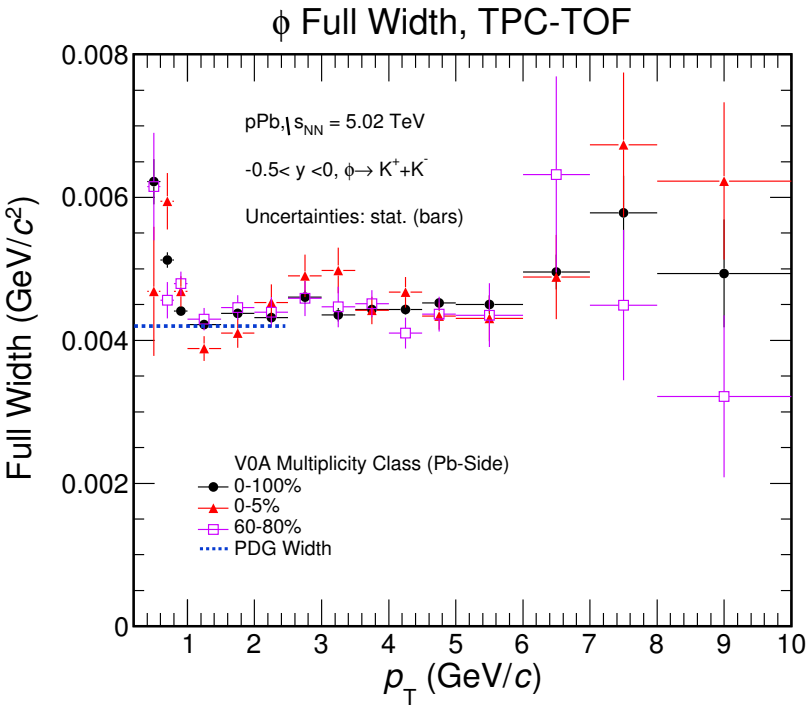

Figure 5.3: Width of the ϕ mesons measured in Minimum bias, 0-5% and 60-80% multiplicity ranges. Only statistical uncertainties are shown.

5.3 Systematic Uncertainties Analysis

Often, systematic uncertainties are neither very clearly defined nor well separated from statistical uncertainties. Sometimes the two uncertainties even become mixed, for example in trigger efficiencies, which may be partially determined from data statistics. Moreover, in many analyses, so-called 'external errors' from external input values, 'theory errors' from theoretical input or other error sources are separated from the 'experimental' systematic uncertainty. A standard definition of systematic uncertainties is the following[22]:

> Systematic uncertainties are all uncertainties that are not directly due to the statistics of the data

With this definition, also statistical uncertainties of trigger efficiencies, measured from data, and detector acceptances, determined from Monte Carlos(MC) simulation, are considered as systematic errors. This may seem strange, but it appears justified when considering that these uncertainties may still be reduced after the data-taking by further Monte Carlo

production or by smarter methods of determining a trigger efficiency. I will use a pragmatic definition of systematic uncertainties, which better fits the purpose of this work[22]:

> Systematic uncertainties are measurement errors which are not due to statistical fluctuations in real or simulated data samples

With this definition, a list of typical sources of systematic errors and biases in high energy physics can be written:

- badly known detector acceptances or trigger efficiencies;
- incorrect detector calibrations;
- badly known detector resolutions;
- badly known background;
- uncertainties in the simulation or underlying theoretical models;
- uncertainties on input parameters like cross sections, branching fractions, lifetimes, the luminosity, and so on(often called 'external uncertainties');
- computational and software errors;
- personal biases towards a specific outcome of an analysis;
- other usually unknown effects on the measurement.

Obviously, in particular the last three sources of systematic are difficult to asses, but also the other items on the list are sometimes difficult to find and to estimate. In this section the procedure followed to obtain the systematic uncertainties will be described. It consist basically in varying many times the possible permutations of the analysis parameters such as: fit region, combinatorial and residual background, PID cuts, etc. The same analysis is repeated for each p_{T} and multiplicity range, giving several measurements for the ϕ yield. The general strategy for evaluating systematic uncertainties is described in the next points:

1. Choose one set of parameters for the analysis as "default".
2. Observe deviation in the yield between the default system and the system when one of the parameters is changed.

3. The systematic uncertainty is calculated for a given source as the RMS[1] deviation of the available sources.

4. The total systematic uncertainty, taking into account all the different sources, is the sum in quadrature of each source.

5.3.1 Systematic Uncertainties of the Yield

Before starting to review all the permutation in the parameters of the systematic uncertainties analysis it is good to recall the default parameters used to obtain the ϕ spectra.

Default Parameters:

- **PID cut:** $3\sigma_{TPC-TOF}$.
- **Combinatorial Background and Normalization Region:** Mixed event normalized to the invariant-mass region $1.04 < M_{\phi} < 1.06$ GeV/c^2.
- **Fit Region:** $0.99 < M_{\phi} < 1.09$ GeV/c^2.
- **Peak Fit:** Voigtian function, where the width parameter is fixed to the vacuum(PDG) value 4.26 MeV/c^2.
- **Yield Extraction Method:** Integrating the invariant-mass histogram (bin counting).

5.3.1.1 Detailed description of each source

In order to obtain a more reliable estimation of the uncertainties, the systematic errors have been computed as the Root Mean Square (RMS) of the measurements set, where RMS is defined as

$$\sigma_x = \sqrt{\frac{1}{N}\sum_{i=1}^{N} x_i^2}, \tag{5.3}$$

where x_i is the measurement, N is the number of measurements in the sample. In this section, the uncertainties will be denoted with "U" and a subscript describing the type of systematic.

[1] Root Mean Square

PID Cuts (U_{PID}): The systematic uncertainty U_{PID} accounts for a non-ideal PID response of the detector, which would result in a deviation in the ϕ yield when different PID cuts are applied. The TPC and TOF analysis is based on $3\sigma - cut$ for the kaons selection. In order to check the systematic effects related to the PID selection, 4σ cut has been compared to the default value.

Normalization Region (U_{NR}): The systematic uncertainty of the normalization region, is related to the invariant mass region where the mixed events distribution is scaled to subtract the combinatorial background. It is obtained by taking the RMS deviation from the default measurement(Normalization Region 0) and the Normalization Regions 1 and 2 listed below:

- **Normalization Region 0:** $1.04 < M_{K^+K^-} < 1.06$ GeV/c^2.
- **Normalization Region 1:** $0.995 < M_{K^+K^-} < 1.01$ GeV/c^2.
- **Normalization Region 2:** $0.995 < M_{K^+K^-} < 1.006$ and $1.04 < M_{K^+K^-} < 1.06$ GeV/c^2.

Fit Region (U_{FR}): The U_{FR} uncertainty is the difference in the yields when different regions for the residual background fit are used. The default Region 0 is compared with Region 1, 2 and 3. The Voigtian function (Γ fixed) together with the residual background (pol2) are fitted in each region giving variations to the yields, then the RMS of the available values gives the systematic uncertainty.

- **Fit Region 0:** $0.99 < M_{K^+K^-} < 1.09$ GeV/c^2.
- **Fit Region 1:** $0.995 < M_{K^+K^-} < 1.06$ GeV/c^2.
- **Fit Region 2:** $1.0 < M_{K^+K^-} < 1.07$ GeV/c^2.
- **Fit Region 3:** $0.99 < M_{K^+K^-} < 1.07$ GeV/c^2.

Residual Background Fit (U_{RB}): The use of a different polynomial function to fit the residual background gives the (U_{RB}) uncertainty. The default yield is extracted using a quadratic fit function and then the systematic uncertainty is calculated when a linear function fit is used.

Peak Fit (U_{PF})**:** This uncertainty accounts for differences observed in the yield when different peak fit functions are used, it mainly consist in varying the fit function parameters. The default measurement Voigt0 fit is compared to the Voigt1, Voigt2 and Voigt3, as listed below:

- **Voigtian 0:** The resolution is allowed to vary freely and the width parameter is fixed to the vacuum value 4.26 MeV/c^2.
- **Voigtian 1:** The resolution is fixed to the value σ_{histo}.
- **Voigtian 2:** The resolution is fixed to the value σ_{voi}.
- **Voigtian 3:** The resolution is fixed to the value σ_{gauss}.

The calculation of $\sigma_{histo}, \sigma_{voi}$ and σ_{gauss} is described in Appendix.0.1.

Peak Yield Extraction Method (U_{Yi})**:** The RMS in the yield due to the extraction method between integrating the histogram (bin counting) used as default, and integrating the fit function gives the systematic uncertainty (U_{Yi}).

Tracking (U_{track})**:** The value of the Global Tracking Efficiency uncertainty is borrowed from the identified charged particles analysis [27], where it is assigned 3% for a single track and for the case of ϕ the value is $U_{track} = 6\%$.

Material Budget (U_{MB})**:** The material supporting the detectors and their misalignment constitute the 'dead zones' in which the detector is not sensitive to the particle passage. This is taken into account by the U_{MB} systematic uncertainty which is a p_{T} dependent. And the value assigned to the ϕ depends on the p_{T} of each kaon, the kaon individual MB uncertainty is obtained from the identified charged particles analysis in p-Pb collisions at $\sqrt{s_{NN}} = 5.02$ TeV [27]. The left plot in the figure 5.4 shows the systematic percentile values as a function of p_{T}.

Hadronic Interactions (U_{HI})**:** The uncertainty on the hadronic interaction cross section is a p_{T} dependent uncertainty where, as the (U_{MB}), the contribution of each kaon to the total p_{T} of the ϕ is taken into account to calculate this uncertainty. The histograms from figure 5.5 are calculated using the information from each of the kaon daughters, by using Monte Carlo simulations.

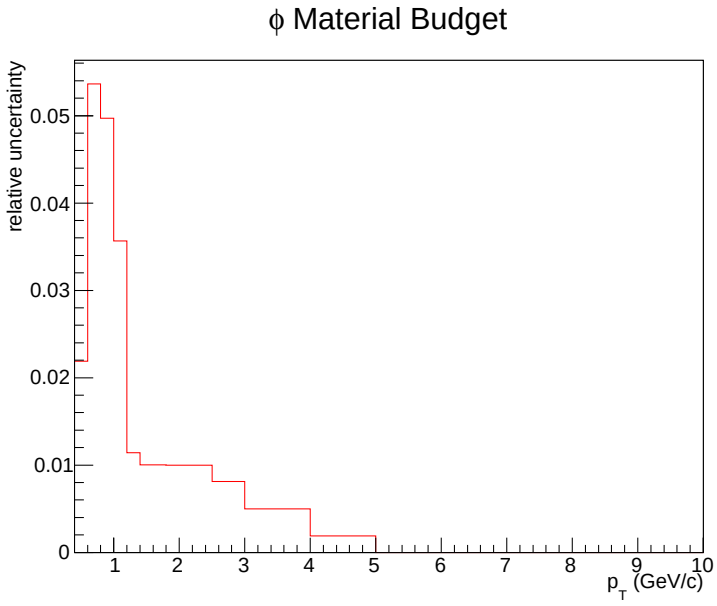

Figure 5.4: p_{T} dependent systematic uncertainty due to material budget(MB) for the ϕ.

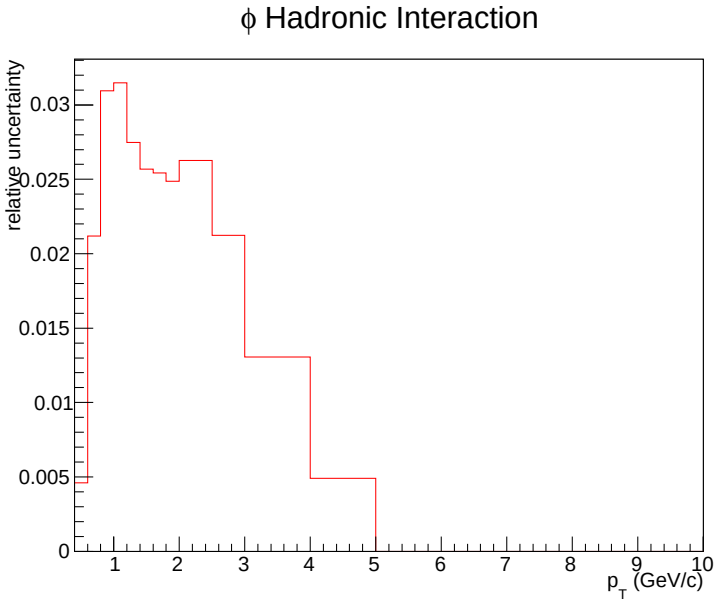

Figure 5.5: p_{T} dependent systematic uncertainty due to hadronic interaction cross section for the ϕ.

Analysis Cuts U_{TrkC}: The systematic uncertainty related to the analysis cuts is calculated by varying some of the StandardITSTPCTrackCuts2011, it is a p_{T} dependent uncertainty that in average is around 2%, the figure 5.6 shows the percentage value of this systematic as a function of p_{T}. The variations used to calculate the U_{TrkC} uncertainty are listed below:

- *Chi 2 in ITS:* 30 and 45 **(36 is default)**
- *Chi 2 in TPC:* 3 and 5 **(4 is default)**
- *MinNCrossedRowsTPC:* 60 and 80 **(70 is default)**
- *DCA-Z:* 1 and 3 **(2 is default)**
- *DCA-XY:* 5 and 9 **(7 is default)**

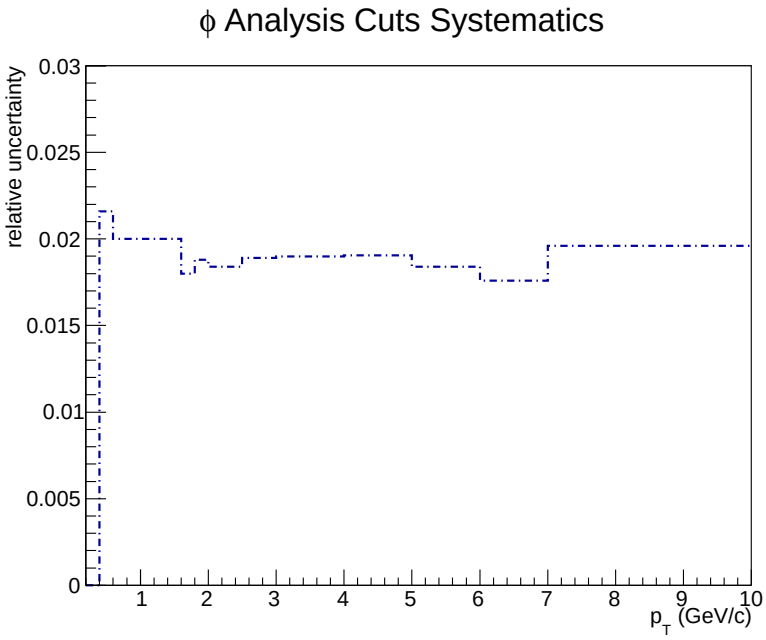

Figure 5.6: p_{T} dependent systematic uncertainty due to analysis cuts variations for the ϕ.

Total Systematic Uncertainty (U_{total})**:** The total systematic uncertainty is the sum in quadrature of all the sources listed above. All these quantities, except for U^2_{HI}, U^2_{MB} and U^2_{TrkC}, are calculated in each multiplicity range.

$$U_T = \sqrt{U^2_{PID} + U^2_{NR} + U^2_{FR} + U^2_{RB} + U^2_{PF} + U^2_{Yi} + U^2_{TE} + U^2_{MB} + U^2_{HI} + U^2_{TC}} \tag{5.4}$$

Smoothing

Some of the raw systematic uncertainties exhibit fluctuations from p_{T} bin to another, but we are expecting that the uncertainties behave more uniform. Then the spikes and dips in the systematic uncertainties have to be smoothed. This is done by comparing the problematic p_{T} bins to the values from the Minimum Bias (0-100)% systematic uncertainty, which is expected to be uniform. Then the (0-100)% value is changed to the problematic one in the multiplicity range, turning the dips and spikes to a more realistic value. The figure 5.7 shows the smoothed systematic uncertainties percentage values for the Minimum Bias measurements and the figure 5.8 shows the same for all multiplicity bins.

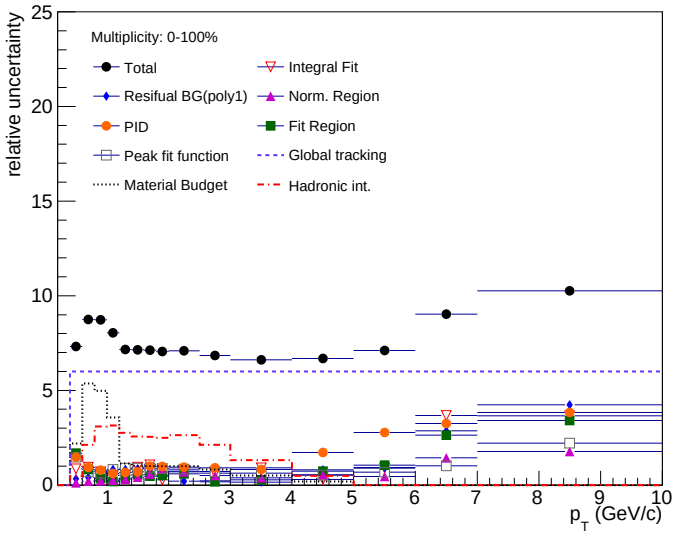

Figure 5.7: Percentage of the systematic uncertainties for each source in 0-100% multiplicity bin, using the combined TPC-TOF information.

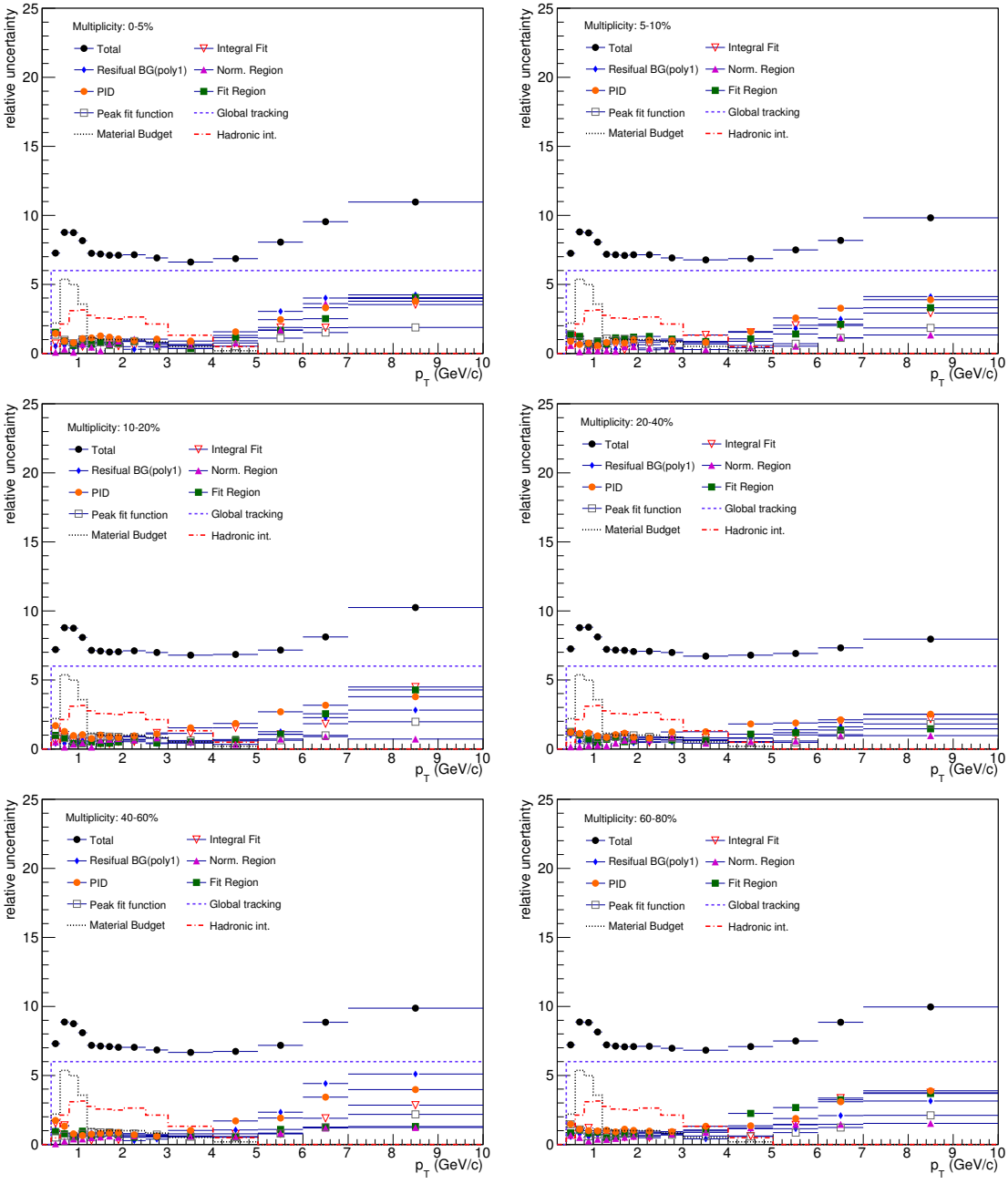

Figure 5.8: Fractional smoothed systematic uncertainties for each multiplicity range and for each systematic source.

After having the fractional systematic uncertainty for all the multiplicity and p_{T} bins, then the ϕ spectra for minimum bias (0-100%) is showed in figure 5.9 and as a function of multiplicity is shown in figure 5.10.

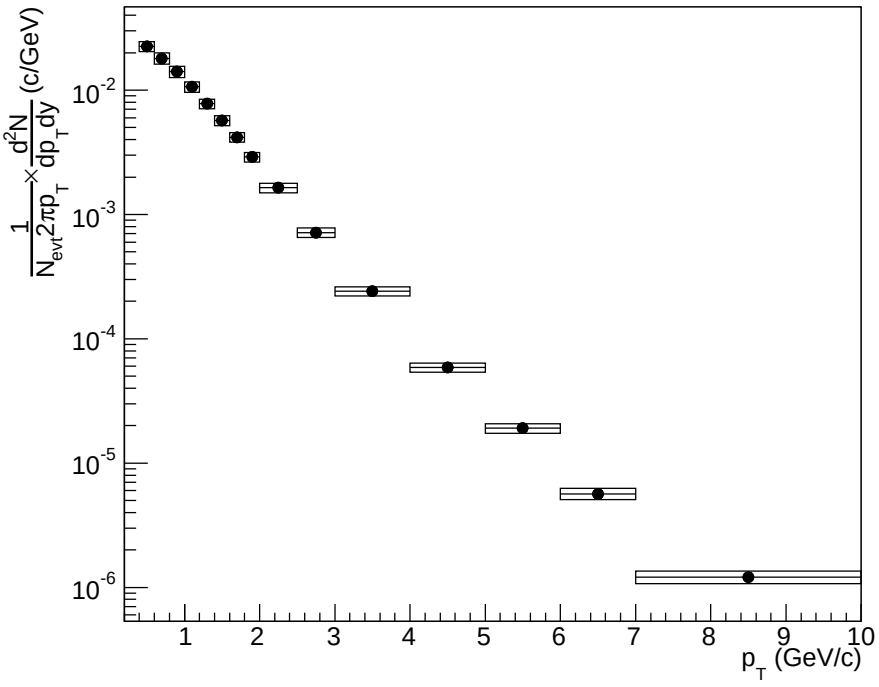

Figure 5.9: Fully corrected spectra for $\phi(K^+K^-)$ using the combined TPC-TOF information, corresponding to minimum bias. Statistical uncertainties (bars) and systematic uncertainties (boxes).

5.3.2 Fits to ϕ Spectra

In order to obtain additional information from the ϕ meson production in p-Pb collision, the ϕ spectra ($d^2N/dp_{\mathrm{T}}dy$) is fitted by some functions that give us details such as the ϕ integrated yield (dN/dy). Three functions are used, the first one is a power law, sometimes called Hagedorn or modified Hagedorn [29]:

$$x \times A \times \left(1 + \frac{x}{p_{t0}}\right)^{-n} \tag{5.5}$$

The histogram is only fit in the region $0.4 < p_{\mathrm{T}} < 10.0$ GeV/c, giving better fit at high

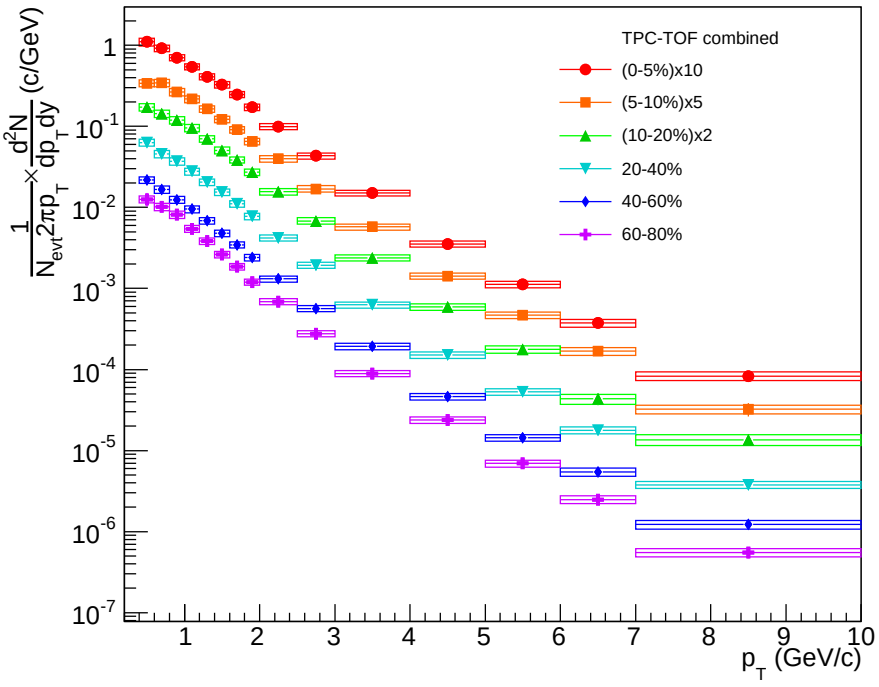

Figure 5.10: Fully corrected spectra for $\phi(K^+K^-)$ using the combined TPC-TOF information as a function of multiplicity. Statistical uncertainties are shown in bars and systematic uncertainties are shown in boxes.

p_{T} but at low p_{T} the fit is not good. Thus the power law function is only used as a cross check, and not for getting information.

Second, a Boltzmann-Gibbs blast wave function [31] is used to fit the data:

$$p_{\mathrm{T}} \times Am_T \int_0^1 xI_0\left(\frac{p_{\mathrm{T}}}{T}\sinh\tanh^{-1}\left[\beta_s x^n\right]\right) K_1\left(\frac{m_T}{T}\cosh\tanh^{-1}[\beta_s x^n]\right) dx, \tag{5.6}$$

where I_0 and K_1 are modified Bessel functions of the first and second kind, respectively. The histogram is fit over the data range, $0.4 < p_{\mathrm{T}} < 10.0$ GeV/c. This function gives a good description of the data in all momentum range, thus this will be compared with the third function; a Lévy-Tsallis function [32]-[33]:

$$p_{\mathrm{T}} \times \frac{A(n-1)(n-2)}{nT[nT+M(n-2)]\left[1+\frac{m_T-M}{nT}\right]^{-n}} \tag{5.7}$$

where A is a parameter that gives the integral of the function. Again, the function is fit over the data range and extrapolated above and below the data. The Lévy-Tsallis function is used as default fit function. The figures 5.11 and 5.12 show the three function fitted to the data points for (5-10)% and (60-80)% multiplicity ranges.

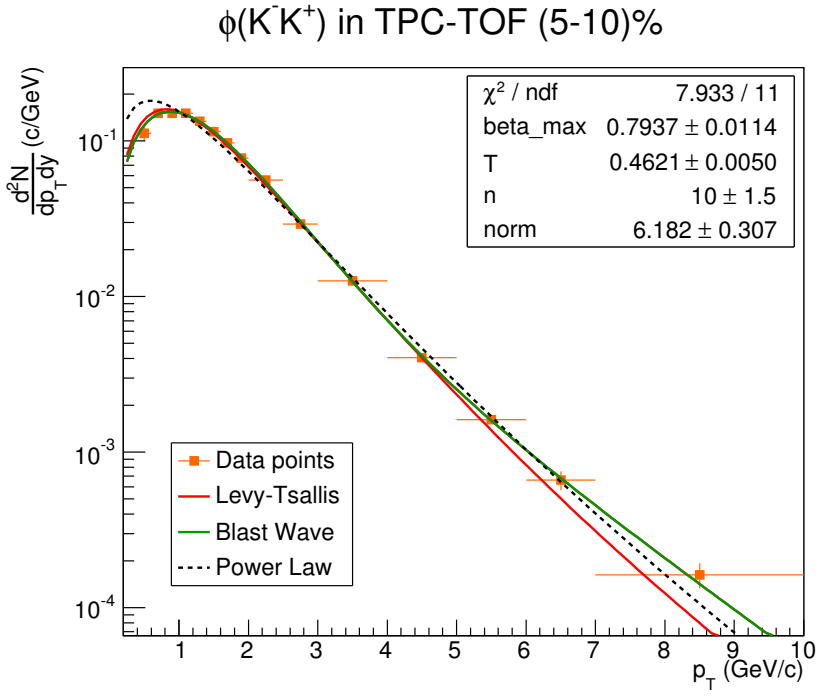

Figure 5.11: Fits to the corrected ϕ spectra ($d^2N/dp_{\mathrm{T}}dy$) in the 5-10% multiplicity bin.

5.3.3 Integrated Yield and Particle Ratios

The method used to obtain the total dN_ϕ/dy depends on the p_{T} region and is summarized in the next points:

- **Below Data:** Low p_{T} region, $0 < p_{\mathrm{T}} < 0.4$ GeV/c, from the extrapolation of the Lévy-Tsallis fit the dN/dy is obtained by integrating the function.
- **Data:** Region where data points are present, $0.4 < p_{\mathrm{T}} < 10.0$ GeV/c, dN/dy is obtained by integrating the data.
- **Above Data:** High p_{T} region, $10.0 < p_{\mathrm{T}} < 30.0$ GeV/c, dN/dy obtained by integrating the extrapolation of Lévy-Tsallis fit.

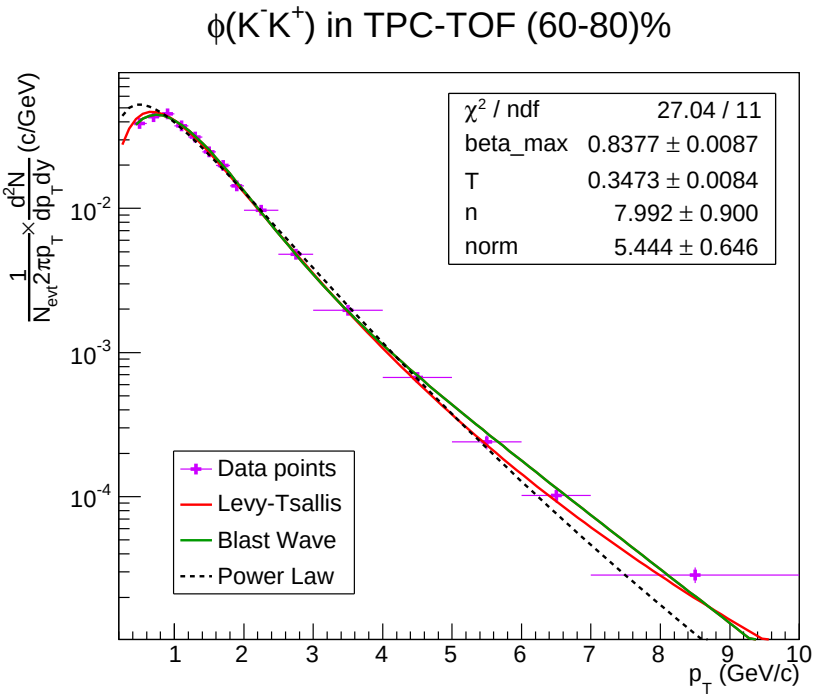

Figure 5.12: Fits to the corrected ϕ spectra ($d^2N/dp_{\mathrm{T}}dy$) in the 60-80% multiplicity bin.

The total dN/dy is then the sum of the three regions described before. The statistical and systematic uncertainties are calculated by re-fitting the data when the data point are moved up and down to the errors limits, as it is shown in the figure 5.13. Then the maximum difference between $(dN/dy)_{high} - (dN/dy)_{data}$ and $(dN/dy)_{data} - (dN/dy)_{low}$ is taken as the statistical or systematic uncertainty for the $(dN/dy)_{data}$, depending the case. The same procedure is repeated for all the multiplicities.

Since the global tracking efficiency is correlated among p_{T} bins it was taken out from the ϕ spectra and then the integrated yield is calculated with this spectra. Then the 6% from the global tracking efficiency is added in quadrature, as $0.06 \times (dN/dy)$, to all the systematic uncertainties. The systematic due to the fit function is obtained by comparing the $(dN/dy)_{fit}$ from Lévy-Tsallis and blast wave function, and the difference is added in quadrature to the data systematic uncertainty $(dN/dy)_{data}$.

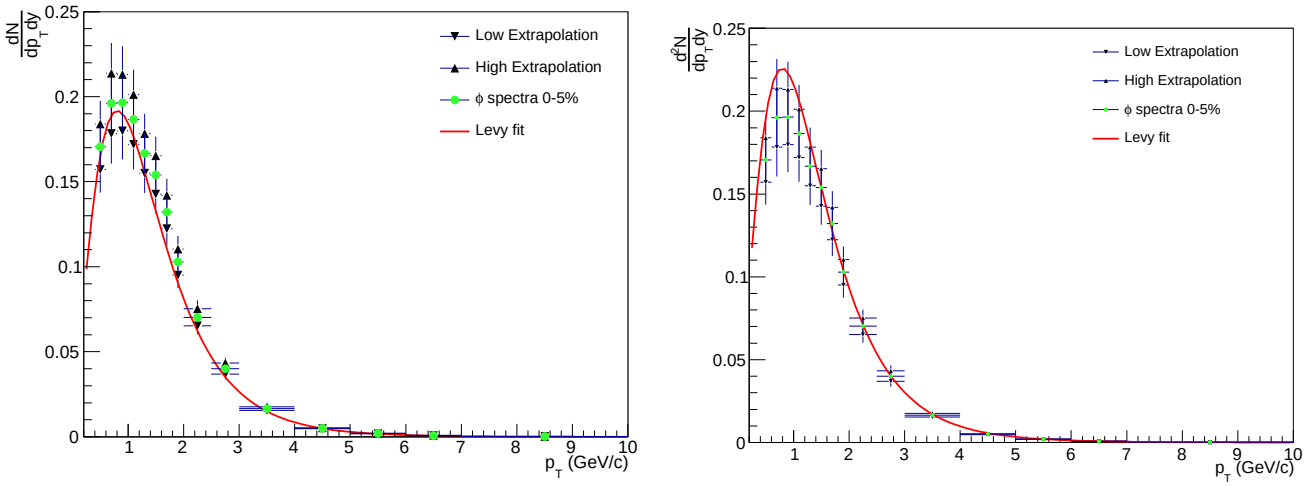

Figure 5.13: **Left:** ϕ points, for 0-5%, moved down to the systematic unc. limit. **Right:** ϕ points moved up to the systematic unc. limit. The red curve is the Levy fit to each spectra.

The mean transverse momentum is obtained as:

$$\langle p_{\mathrm{T}} \rangle = \frac{\langle p_{\mathrm{T}} \rangle I_{ext} + \Sigma_{ibin} \overline{p}_{\mathrm{T,ibin}} \mathrm{d}p_{\mathrm{T,ibin}} I_{ibin}}{I_{data} + I_{ext}} \tag{5.8}$$

where $\langle p_{\mathrm{T}} \rangle$ and I_{ext} are respectively the mean transverse momentum for the extrapolation region(from fitted function) and the integral of the fitted function in the extrapolation region, $\overline{p_{\mathrm{T}}}$ is the p_{T} bin center of the ibin-th, $\mathrm{d}p_{\mathrm{T,ibin}}$ is the bin with and I_{ibin} is the yield of the ibin-th. For the systematic uncertainty on the $\langle p_{\mathrm{T}} \rangle$ similar procedure as described before for the dN/dy is followed. The figure 5.14 show the ϕ integrated yield(left) and the mean p_{T}. In the next chapter this results will be discussed.

In order to study the multiplicity dependence, the selected events are divided into six event classes, based on cuts on the total charge deposited in the VZERO-A detector (V0A). The corresponding fractions of the data sample in each class are summarized in Table 5.1. The mean charged-particle multiplicity densities ($\langle \mathrm{d}N_{ch}/\mathrm{d}\eta \rangle$) within $|\eta_{lab}| < 0.5$ corresponding to the different event classes are also listed in the table. These are obtained using the method presented in [34] and are corrected for acceptance as well as for contamination by secondary particles.

Event Class	V0A range(arb. unit)	$\langle \mathrm{d}N_{ch}/\mathrm{d}\eta \rangle_{\lvert\eta_{lab}\rvert<0.5}$
0-5%	>227	45±1
5-10%	187-227	36.2±0.8
10-20%	142-187	30.5±0.7
20-40%	89-142	23.2±0.5
40-60%	52-89	16.1±0.4
60-80%	22-52	9.8±0.2
80-100%	<22	4.4±0.1

Table 5.1: Definition of the event classes as fractions of the analyzed event sample and their corresponding $\langle \mathrm{d}N_{ch}/\mathrm{d}\eta \rangle$ within $|\eta_{lab}| < 0.5$ (systematic uncertainties only, statistical uncertainties are negligible). Table values taken from [27].

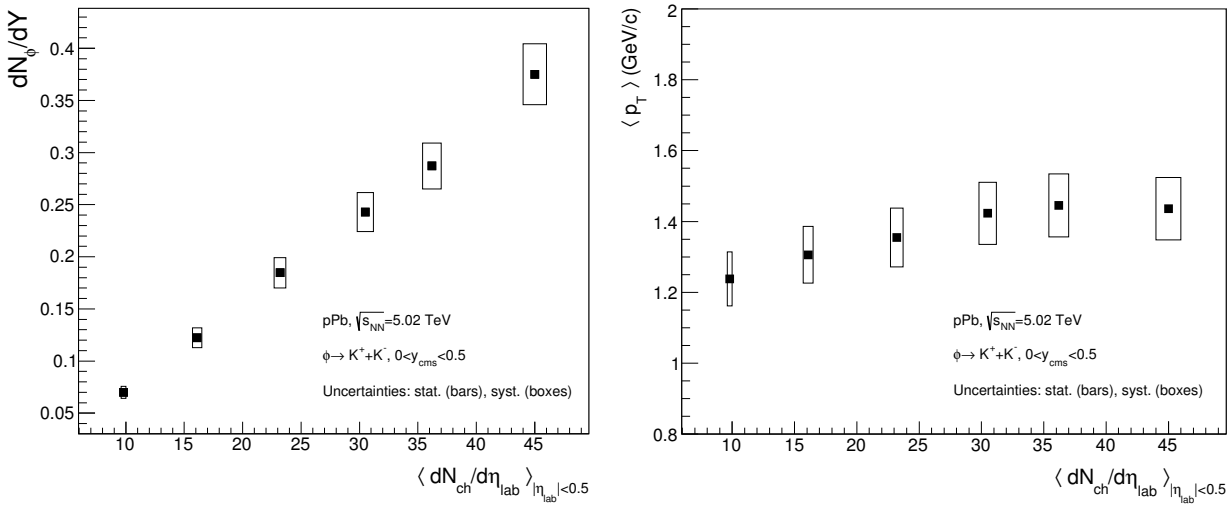

Figure 5.14: **Left:** ϕ integrated yield as a function of multiplicity. dN_ϕ/dy vs $dN_{ch}/d\eta$. **Right:** ϕ mean p_T ($\langle p_\mathrm{T} \rangle$) as a function of multiplicity. Systematic uncertainties (boxes), statistical uncertainties (lines).

5.4 Analysis Combination

In the ALICE experiment several people work on the same analysis using different techniques, in this manner the analyses have to converge to the same results. This ϕ analysis is not the exception, besides this TPC-TOF analysis presented in this thesis, two other analysis were performed simultaneously and in this section the merge procedure of the three analysis results is presented.

The three analysis to obtain the ϕ meson spectra and the people involve in each analysis are listed below, together with the respectively ALICE analysis note link:

- **TPC analysis**: By Ajay K. Dash,
  https://aliceinfo.cern.ch/Notes/node/264.
- **TPC-TOF analysis**: By Edgar P. Lezama, described in this thesis.
  https://aliceinfo.cern.ch/Notes/node/222
- **No PID analysis**: By Viktor Riabov, M. Malaev and Y. Ryabov,
  https://aliceinfo.cern.ch/Notes/node/214.

The three analysis have a good agreement between each other, the figure 5.15 shows the comparison of the global fit[1] with each different measurement method for the minimum bias case (all multiplicity comparison have a good agreement too). Since the No-PID method can provide better description at high p_{T} compared to the TPC-TOF method, the final ϕ spectra is composed by TPC-TOF points up to $p_{\mathrm{T}} = 3$ GeV/c and above that momentum the No-PID results are used, the figures 5.16 and 5.17 show the combined spectra for minimum bias and all multiplicity cases respectively.

[1] Fit to all the data points

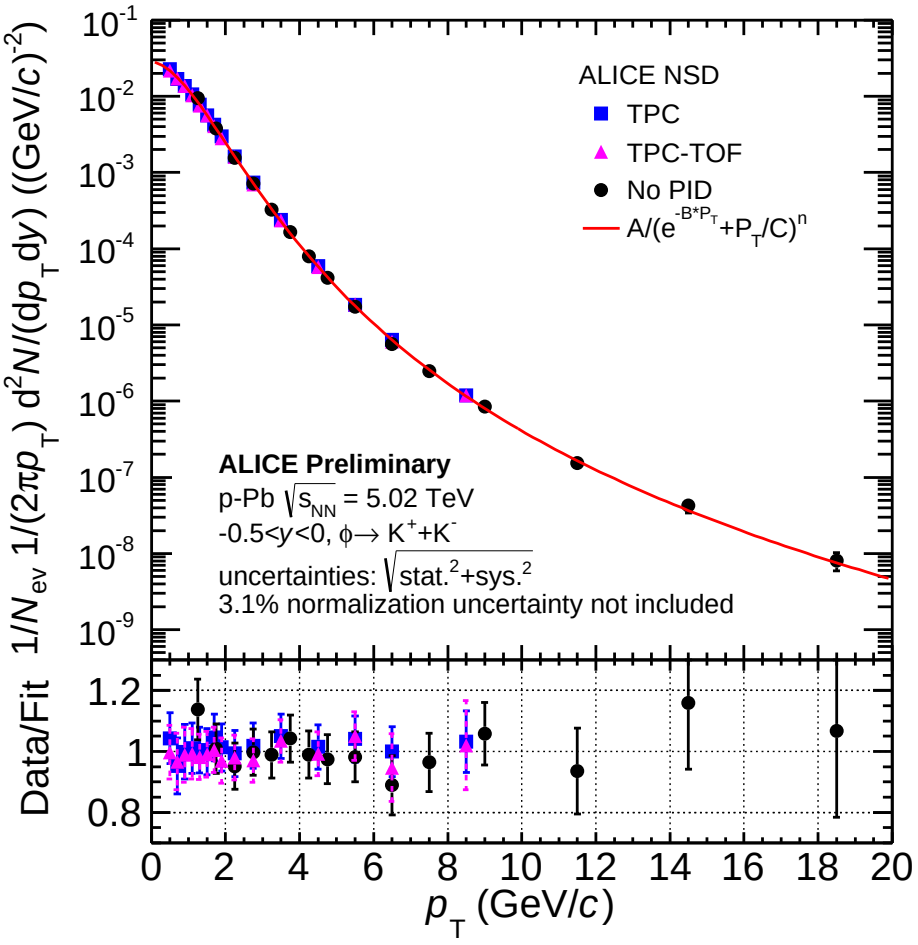

Figure 5.15: Comparison between the three different methods to obtain the ϕ spectra. The fit is compared to the data point at the bottom of the plot.

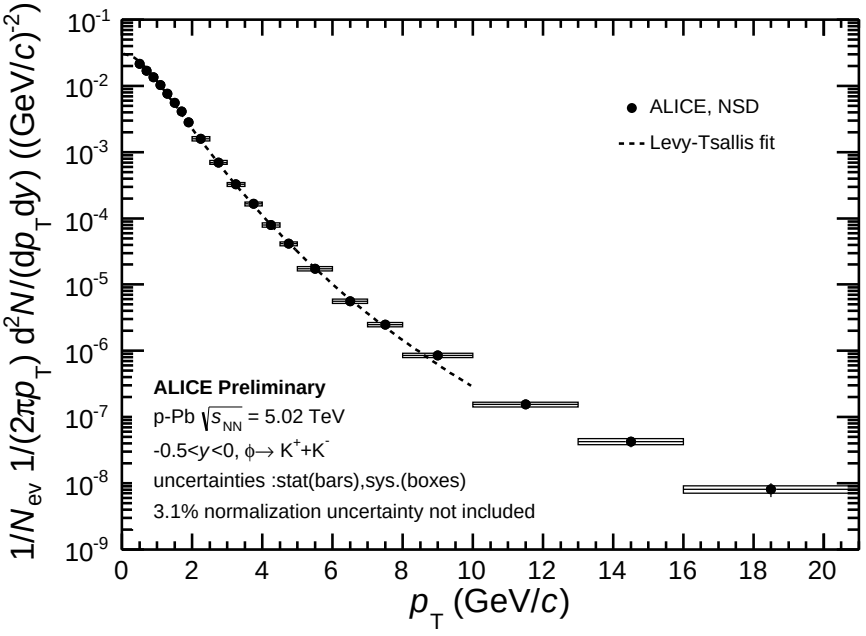

Figure 5.16: Combined ϕ invariant spectra for minimum bias measurement, Levy-Tsallis fit function is shown. Statistical uncertainties (bars), Systematic uncertainties (boxes).

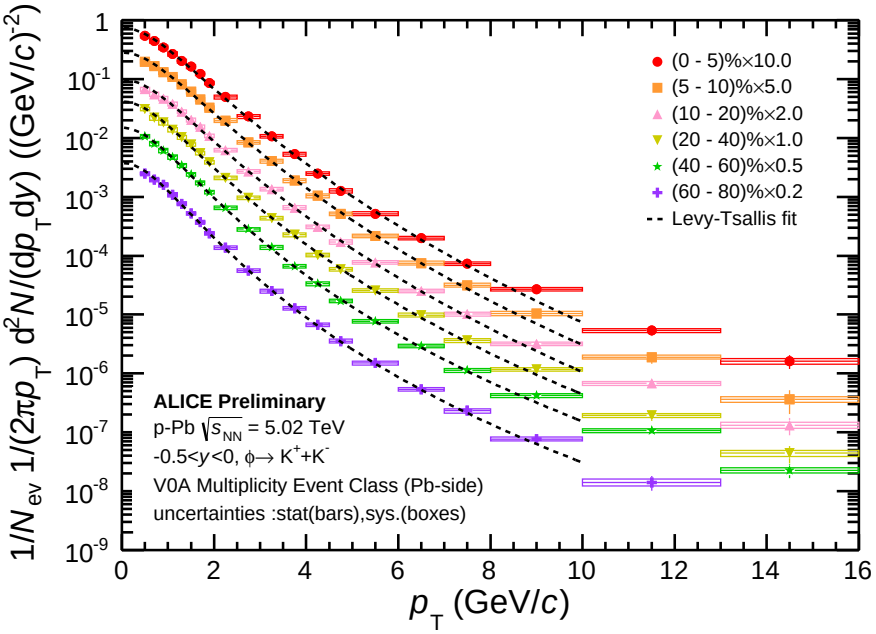

Figure 5.17: Combined ϕ invariant spectra for six multiplicity ranges, and the respectively Levy-Tsallis fit functions. Statistical uncertainties (bars), Systematic uncertainties (boxes).

Chapter 6

Discussion of Results

Using the ϕ combined spectra shown in figure 5.16 and 5.17, we can obtain the ϕ(1020) integrated yield as a function of multiplicity, it means the yield obtained from the fit and the data points of each spectra. The figure 6.1 shows this information. From that figure is clear that the ϕ meson production has an increasing trend when one goes from peripheral to central collisions.

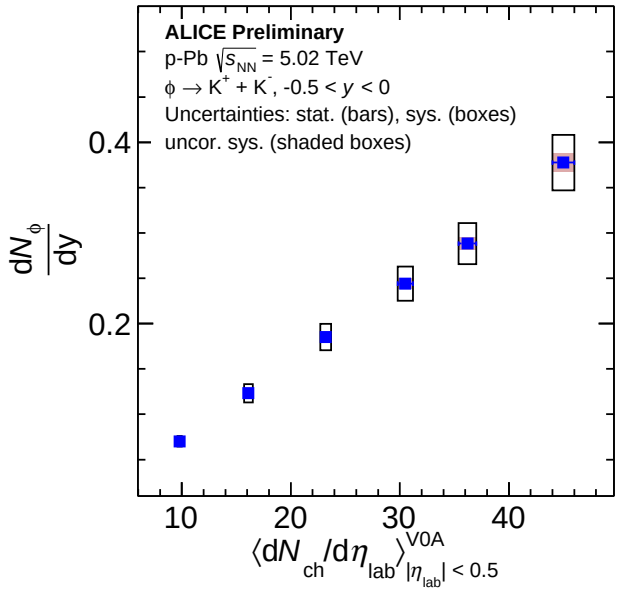

Figure 6.1: ϕ integrated yield(dN_ϕ/dy) as a function of multiplicity. Statistical uncertainties(bars), systematic uncertainties(boxes) and uncorrelated systematic (shaded boxes).

The mean transverse momentum $\langle p_{\mathrm{T}} \rangle$ for the ϕ resonance, as well as for other particles, are presented in the figure 6.2 for two collision systems; pp at $\sqrt{s} = 7$ TeV and p-Pb at $\sqrt{s_{NN}} = 5.02$ TeV. Similar to what was observed in Pb-Pb[35], the p-Pb collisions exhibit the same increasing trend for the ϕ as well as for other hadrons ($\mathrm{K}^{*0}, \Lambda, p, \mathrm{K}^{\pm}, \pi^{\pm}$). While the $\langle p_{\mathrm{T}} \rangle$ of stable particles seem to follow a mass ordering, the resonances (ϕ, K^{*0}) do not, is clear that their mean transverse momentum is larger than p and Λ mean p_T. Similar mass ordering deviation for resonances is observed in pp collisions. From the mean p_{T} plot one can note that the baryon mean p_{T} (p and Λ) is higher than the meson mean p_{T} ($\mathrm{K}^{\pm}$, K^0_s and $\pi^{\pm}$), but for the $\phi(1020)$ and K^{*0} the mean p_{T} values are similar to the baryon ones. Since the masses of p($\mathrm{m_p} = 938$ MeV/c^2), K^{*0}($\mathrm{m_{K^{*0}}} = 891$ MeV/c^2), ϕ($\mathrm{m_\phi} = 1019$ MeV/c^2) and Λ($\mathrm{m_\Lambda}$=1115 MeV/c^2) are similar one would expect that the $\langle p_{\mathrm{T}} \rangle$ values should be consistent with each other but this was not found.

The $\langle p_{\mathrm{T}} \rangle$ values for pp collision are consistent with peripheral p-Pb collisions, following the same mass ordering as observed in p-Pb collisions. In the case of K^{*0} the pp value is in between the multiplicity ranges (60-80)% and (80-100)% but in the case of ϕ the most peripheral multiplicity range analysed[1] is (60-80)%.

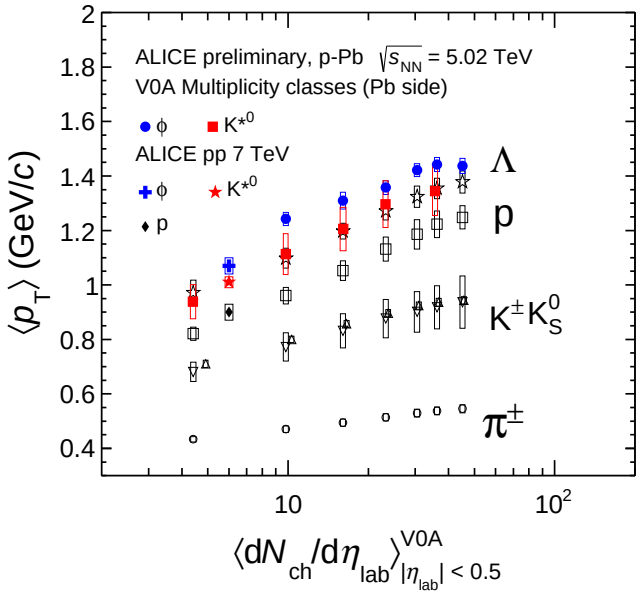

Figure 6.2: Mean transverse momentum of $\pi^{\pm}, \mathrm{K}^{\pm}, \mathrm{K}^0_s, \mathrm{K}^{*0}_s, p, \Lambda$ and ϕ for two collision systems, pp at $\sqrt{s} = 7$ TeV and p-Pb at $\sqrt{s_{NN}} = 5.02$ TeV.

[1]The future work will add the (80-100)% value.

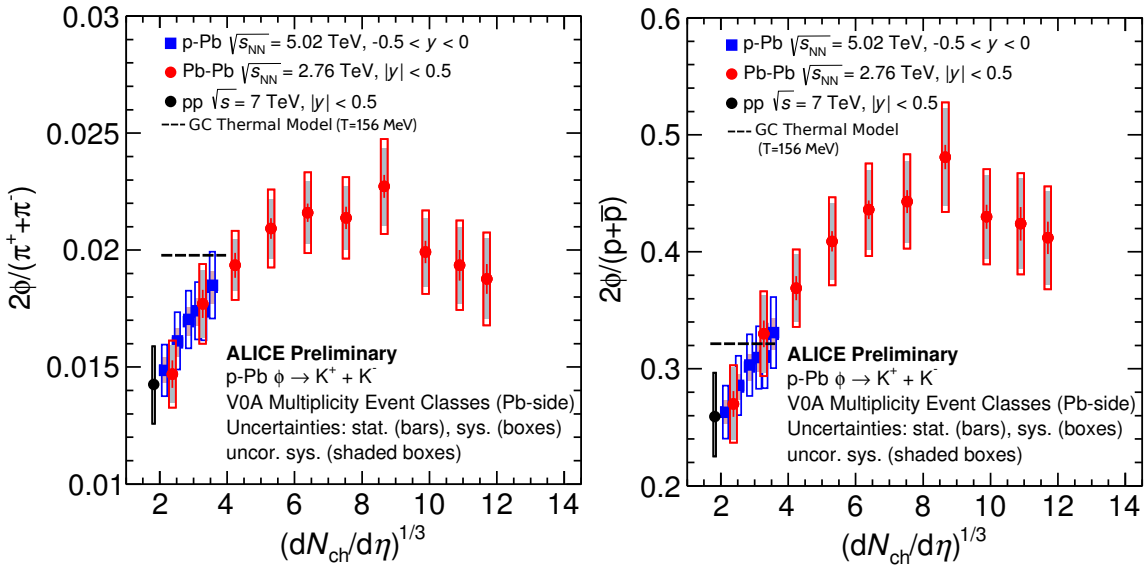

Figure 6.3: **Left:** Ratio ϕ/π as a function of multiplicity $(dN_{ch}/d\eta)^{1/3}$ for the three collision systems: pp, p-Pb and Pb-Pb. **Right:** Ratio ϕ/p as a function of multiplicity $(dN_{ch}/d\eta)^{1/3}$ for the same collision systems described before. Statistical uncertainties(bars), systematic uncertainties(boxes) and uncorrelated systematic (shaded boxes).

To study particle production mechanisms one should compare the p_{T} distributions and the total yields of ϕ mesons to theoretical models and other particle species (with different baryon number, mass, or strange quark content). The ϕ meson is used for these studies because it lives long enough that its yields and p_{T} distributions do not appear to be affected by re-scattering or regeneration in the hadronic phase. The figure 6.3 shows the ratios ϕ/π (Left) and ϕ/p (Right). These ratios are presented as a function of $(dN_{ch}/d\eta)^{1/3}$ (the cube root of the charged-particle multiplicity density), where the p-Pb results are compared with pp and Pb-Pb ones and also compared with the theoretical value given by a grand-canonical thermal model (based in Pb-Pb collisions) with a chemical freeze-out temperature of 156 MeV [37]. From the particle ratios it is clear that the p-Pb collision system follows the same increasing trend as the Pb-Pb results, while the pp point is consistent with the peripheral (60-80%) p-Pb point, feature that was expected because p-Pb is the intermediate collision system between pp and Pb-Pb. One observes a good agreement between p-Pb and Pb-Pb in the region of similar multiplicities.

The left plot in figure 6.4 shows the ratio ϕ/K^- as a function of multiplicity where the

results appear to follow a single trend, independent of collision system and energy. The three systems are consistent within the uncertainties and agree with the thermal model calculation. The right plot of the figure shows that the ϕ/K^- ratio is independent of collision energy and system, from RHIC to LHC energies and the thermal model also agrees within the uncertainties with the Pb-Pb, p-Pb and pp collision systems.

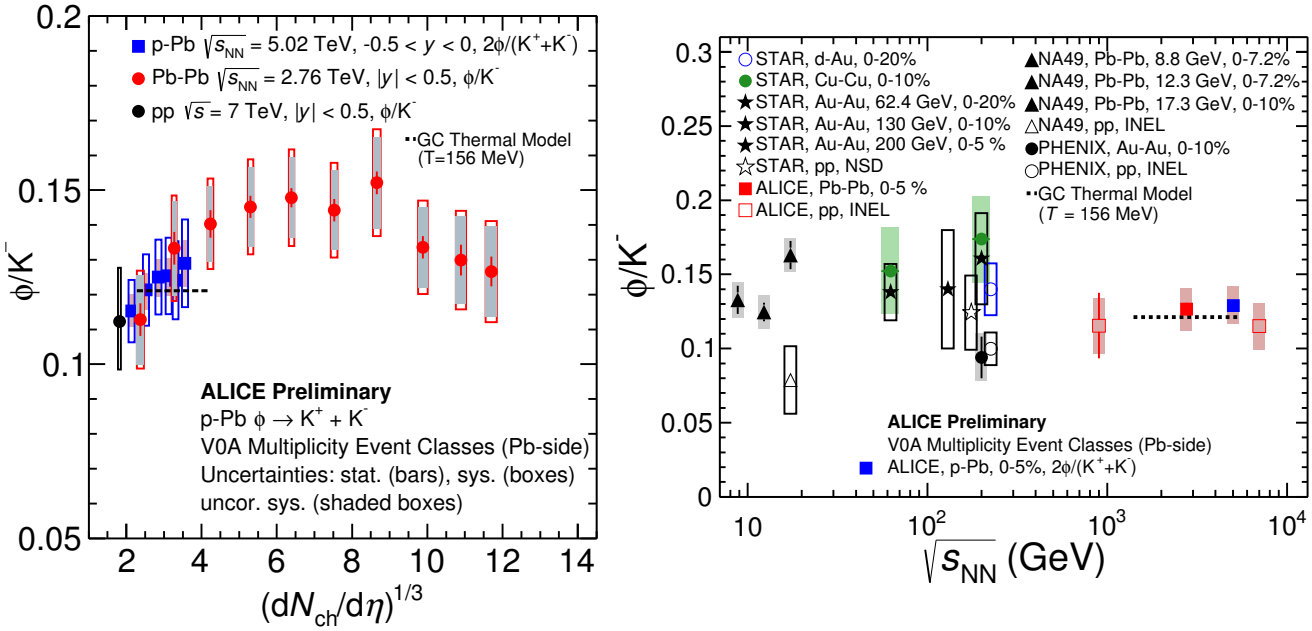

Figure 6.4: **Left:** Ratio ϕ/K^- as a function of multiplicity $(dN_{ch}/d\eta)^{1/3}$ and comparison between pp, p-Pb and Pb-Pb collision systems. **Right:** Ratio ϕ/K as a function of the collision energy($\sqrt{s_{NN}}$) , compared with different collision systems in other experiments. The values given by a grand-canonical thermal model with a chemical freeze-out temperature of 156 MeV are also shown [37]. Statistical uncertainties(bars), systematic uncertainties(boxes) and uncorrelated systematic (shaded boxes) are shown.

Differences in the production mechanisms of baryons and mesons can be studied through baryon-to-meson ratios. If the hadrons produced are subject to hydrodynamical flow, the particle mass plays an important role in determining the shape of the p_{T} distribution. To study this aspect of particle production, the p_{T} distribution of ϕ mesons are compared to protons which is a baryon with a similar mass to the ϕ but different quark content. Figure 6.5 shows $\mathrm{p}/\phi \equiv (\mathrm{p} + \overline{\mathrm{p}})$ as a function of p_{T} for pp, p-Pb and Pb-Pb collision systems. The most central and the most peripheral collisions are presented for p-Pb and Pb-Pb. For the peripheral results, the three collision systems have a good agreement. This similarity is expected because at these multiplicities (centralities) the particle production in p-Pb (Pb-

Pb) should resemble the pp collisions. The 0-5% multiplicity range for p-Pb remains between pp and Pb-Pb (0-10%) up to 2 GeV/c, above that momentum both the pp and p-Pb continue the decreasing trend while the Pb-Pb (0-10%) remains practically flat.

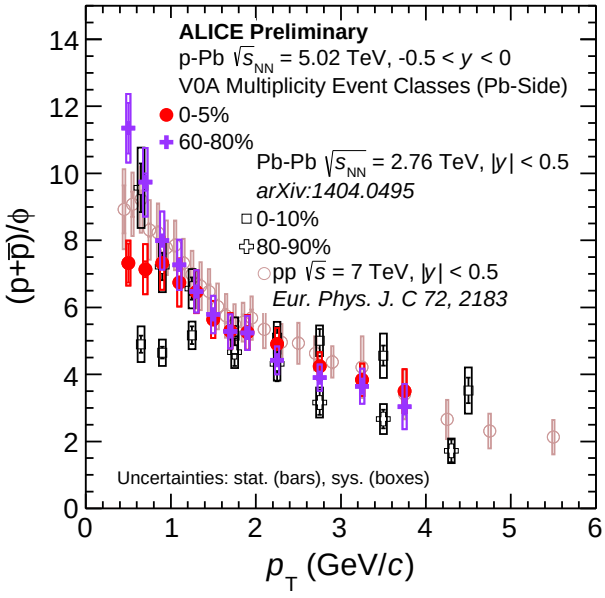

Figure 6.5: Ratio p/ϕ as a function of p_{T} for pp at $\sqrt{s} = 7$ TeV, p-Pb at $\sqrt{s_{NN}} = 5.02$ TeV and Pb-Pb at $\sqrt{s_{NN}} = 2.76$ TeV, comparing central and peripheral intervals.

The figure 6.6 shows the meson-to-meson ratio $\phi/\pi = \phi/(\pi^+ + \pi^-)$ as a function of p_{T}. A very similar increasing trend is observed either is peripheral or central collisions. As it is shown in figure 6.7, the baryon-to-meson ratios p/π in p-Pb(left) and Pb-Pb(right) collisions have a very similar shape compared to the ϕ/π for $p_{\mathrm{T}} < 3$ GeV/c, feature observed also using Pythia at generation level[38]. This indicates that the number of quarks is not an important factor that determines the p_{T} distributions of particles at low and intermediate p_{T} in central collisions.

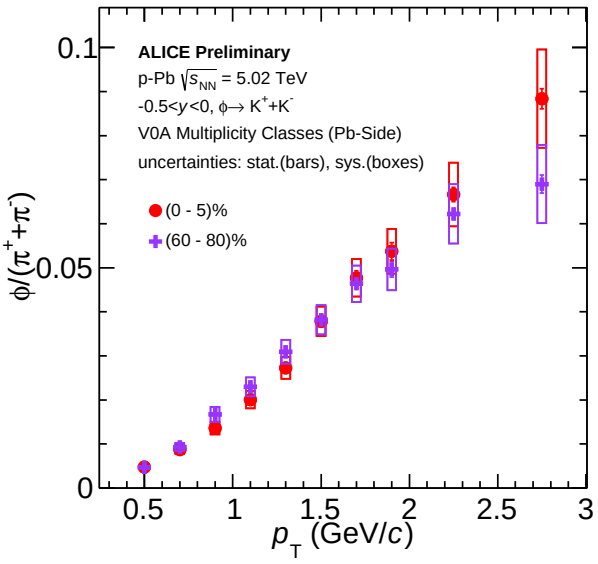

Figure 6.6: Ratio ϕ/π as a function of p_{T} for p-Pb at $\sqrt{s_{NN}} = 5.02$ TeV and comparing central and peripheral measurements.

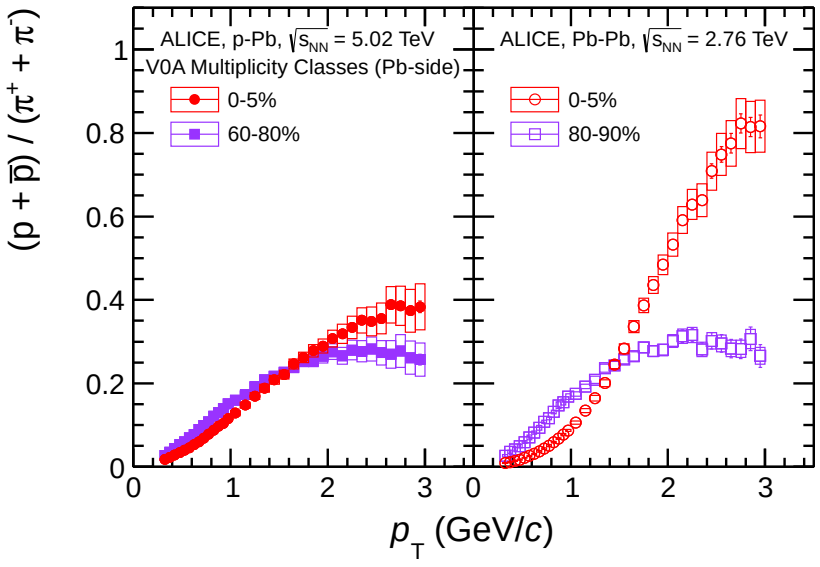

Figure 6.7: Ratio $\mathrm{p}/\pi = (\mathrm{p}+\overline{\mathrm{p}})/(\pi^+ + \pi^-)$ as a function of p_{T} in the rapidity interval $0 < \mathrm{y} < 0.5$ (left panel). The ratios are compared to results in Pb-Pb collisions measured at mid-rapidity, shown in right panel. The empty boxes show the total systematic uncertainty; the shaded boxes indicate the contribution uncorrelated across multiplicity bins. Figure taken from [27].

Chapter 7

Conclusions

In this work the production of the $\phi(1020)$ meson has been measured in p-Pb collision at $\sqrt{s_{NN}} = 5.02$ TeV, in the rapidity region $-0.5 < y < 0$ (Pb side). It was measured through the $\phi \rightarrow K^+ + K^-$ decay channel with a branching ratio of 48.9%. The kaons were selected using the PID capabilities of the TPC and TOF detectors. With the kaons information the ϕ invariant mass is obtained, from which the signal was extracted. The combinatorial background was subtracted from the uneven sign distributions by the Event Mixing technique. The raw yield was extracted by integrating the invariant mass distributions. After the normalizations and corrections to the raw yield, the invariant ϕ spectra are obtained in fifteen p_T intervals and for seven multiplicity ranges; measured by the V0A detector. The systematic uncertainties on the yield were calculated by varying a set of parameters such as: fit settings, residual background function, event mixing normalization region, among others.

The ϕ spectra are fitted by the Levy-Tsallis function in order to obtain information on the integrated yield(dN/dy), which is later compared to other charged particles yields (p, K and π). The $\langle p_T \rangle$ shows an increasing trend for the ϕ as well as for other particles, but for particles of similar masses(K^{*0}, p, ϕ and Λ) the $\langle p_T \rangle$ is not compatible between them which is opposite to the prediction of hydrodynamics. The pp values are found to have the same mass behaviour and consistent with the peripheral p-Pb ones.

Results of particle ratios (ϕ/π, ϕ/p, ϕ/K) as a function of mean charged-particles multiplicity density ($\langle dN_{ch}/dy \rangle$) are compared with pp and Pb-Pb collisions and they are found to be compatible with a common increasing trend. The ratio ϕ/p as a function of p_T for peripheral p-Pb collision(60-80%) is compatible with pp and Pb-Pb(80-90%) and for central p-Pb collision(0-5%) the ratio remains in between peripheral and central Pb-Pb collisions, characteristic that was expected. On the other hand, in meson-to-meson ratio (ϕ/π) there

is practically not difference between central and peripheral p-Pb collisions. Since the behaviour of the ϕ/π is very similar to that of p/π for both p-Pb and Pb-Pb systems we conclude that the important parameter are the masses of the respective particles and not their quark content.

Bibliography

[1] Griffiths, David. *Introduction to Elementary Particles*, 2nd Edition,Wiley-VCH,2004. 1

[2] http://home.web.cern.ch/about/updates/2013/03/new-results-indicate-new-particle-higgs-boson 2

[3] Introduction to High-Energy Heavy-Ion Collisions, C.Y. Wong, World Scientic, 1994 3

[4] F. Halzen and A.D. Martin, Quarks and Leptons, John Wiley and Sons (1984) 5

[5] S. A. Bass et al., Signatures of Quark-Gluon-Plasma formation in high energy heavy-ion collisions:A critical review, J.Phys.G25:R1-R57, 1999. 6

[6] Letessier, Jean and Rafelski, Johann. *Hadrons and Quark-Gluon Plasma*, Cambridge Univesity Press, 2002. 7, 8

[7] J. P. Bailly et al.. Phys. Lett. B195 (1987) 609. 8

[8] J. Rafelski and B. Müller. Phys. Rev. Lett. 48 (1982) 1066 [Erratum: ibid. 56 (1986) 2334]. 9

[9] C. Markert, R.Bellwied, I.Vitev, Phys.Lett. B669:92 (2008) 10

[10] A. G. Knospe (ALICE Collaboration), J. Phys. Conf. Ser. 420, 012018 (2013). 10

[11] Biolcati, Emanuele. *Distribution of hadrons identified with the Inner Tracking System of the ALICE experiment for p-p data*, Ph.D Thesis, Università degli Studi di Torino, Italia, 2011. 11

[12] Tavernier, Stefaan. *Experimental Techniques in Nuclear and Particle Physics*, 1a edición, Springer, 2010.

[13] Perkins, Donald H. *Introduction to High Energy Physics*, 4a edición, Cambridge Univesity Press, 2000. 4, 5

[14] R. Hagedorn, 1965. Statistical thermodynamics of strong interactions at high energies. I. Suppl. Nuovo Cimento, 3, 147. 8, 53

[15] Aguilar-Benitez M. et al. (LEBC-EHS Collaboration), Z. Phys. C 50, 405 (1991). 10

[16] ALICE collaboration, *ALICE forward detectors: FMD, T0 and V0: Technical Desing Report*, CERN-LHCC-2004-025, http://cdsweb.cern.ch/record/781854 15

[17] ALICE Collaboration et al 2004 J. Phys. G: Nucl. Part. Phys. 30 1517. 17, 19

[18] ALICE Collaboration et al. *The ALICE Experiment at the CERN LHC*, 2008, JINST 3 S08002 13

[19] ALICE Experiment, *Detectors of the ALICE experiment*, http://aliceinfo.cern.ch/Public/en/Chapter2/Page3-subdetectors-en.html 17

[20] Breit, G.; Wigner, E. (1936). "Capture of Slow Neutrons". Physical Review 49 (7): 519. doi:10.1103/PhysRev.49.519 33

[21] Olivero, J.J.; R.L. Longbothum (February 1977). "Empirical fits to the Voigt line width: A brief review". Journal of Quantitative Spectroscopy and Radiative Transfer 17 (2): 233236. 34

[22] O. Behnke et al, *Data Analysis in High Energy Physics*, 2012, WILEY-VCH. 44, 45

[23] Kalweit, Alexander Philipp. *Energy Loos Calibration of the ALICE Time Projection Chamber*, Master Thesis, Technischen Universität Darmstadt, Alemania, 2008. 18

[24] W. Blum and L. Rolandi, *Particle Detection with Drift Chambers*. Springer, Berlin, 1998. 23

[25] The ALICE experiment offline project, www.cern.ch/ALICE/Projects/offline/aliroot/Welcome.html. 21

[26] ALICE collaboration (K. Aamodt et al.), The European Physical Journal, C71, Number 6, 1655, 2010. 20

[27] Abelev B I et al. (ALICE Collaboration), Physics Letters B 728, 20, 2014. xix, 28, 48, 58, 67

[28] L. Evans and P. Bryant, JINST 3, S08001 (2008). 26

[29] Nuclear Physics B, Vol. 335, No. 2. (7 May 1990), pp. 261-287 8, 53

[30] K. Nakamura et al. (Particle Data Group), J. Phys. G 37, 075021 (2010). 37

[31] Schnedermann E, Sollfrank J and Heinz U 1993 *Phys. Rev.* C **48** 246275 54

[32] Tsallis C 1988 J. *Stat. Phys.* **52** 479 54

[33] Abelev B I et al. (STAR Collaboration) 2007 *Phys. Rev.* C **75** 064901 54

[34] ALICE Collaboration, B. Abelev, et al., Pseudorapidity density of charged particles pPb collisions at $\sqrt{s_{NN}} = 5.02$ TeV, Phys. Rev. Lett. 110 (2013) 032301. 57

[35] Abelev B I et al. (ALICE Collaboration) 2014 $K^*(892)^0$ *and* $\phi(1020)$ *production in Pb-Pb collision at* $\sqrt{s_{NN}} = 2.76$ *TeV*, http://arxiv.org/abs/1404.0495 43, 63

[36] Harsh Shah, *Detection of* $\phi(1020)$ *meson by the decay* $\phi \rightarrow K^+K^-$ *in AMPT model*, http://www.niser.ac.in/ bedanga/Detection_phi_harsh.pdf 43

[37] J. Stachel, A. Andronic, P. Braun-Munzinger, K. Redlich, 2014, *J. Phys.: Conf. Ser.* **509**, 012019 xix, 64, 65

[38] E. Cuautle, R. Jimenez, I. Maldonado, A. Ortiz, G. Paic and E. Perez, arXiv:1404.2372 [hep-ph].

66

Appdx A

.0.1 Resolution

In this appendix section will be described the way the different variations of resolutions are obtained, but first it is useful to note that M_{gen} is not necessarily the PDG mass: the generated ϕ mesons are assigned masses with a realistic (Breit-Wigner) distribution. And this generated mass is obtained by fitting a Breit-Wigner to the generated histogram in the 0-100% multiplicity bin giving the value: $M_{gen}(BW) = 1.019543 \pm 0.000005$ GeV/c^2 and $\Gamma_{gen} = 4.399 \pm 0.019$ MeV/c^2, and these values are p_{T} independent. The generated mass and the mean mass shift $\langle \Delta M \rangle$ will be used to correct the real mass distribution. The mean mass shift and the resolution histogram are extracted from the "resolution histogram" (ΔM) in the following manners:

- A Gaussian is used to fit the ΔM histogram, where the mean mass shift $\langle \Delta M \rangle$ is the mean parameter of this Gaussian, and the resolution parameter is labeled as σ_{Gauss}.
- The resolution and the mean mass shift are taken directly from the ΔM histogram, without any fitting, then the $\langle \Delta M \rangle_h$ and σ_h are obtained.
- The other option used to get the resolution is to fit the reconstructed histogram with a Voigtian function (width fixed to 4.4 MeV/c^2) where the σ_{voi} is obtained.

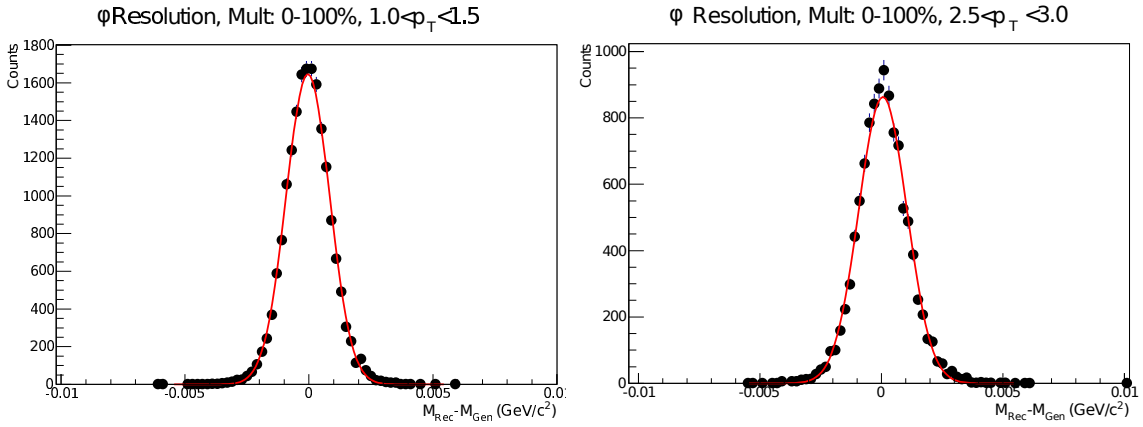

Figure 1: Resolution histogram (truncated Gaussian fit) in the transverse momentum $1.0 < p_{\mathrm{T}} < 1.5$ (left plot) and $2.5 < p_{\mathrm{T}} < 3.0$ (right plot), both in the multiplicity bin $0 - 100\%$.

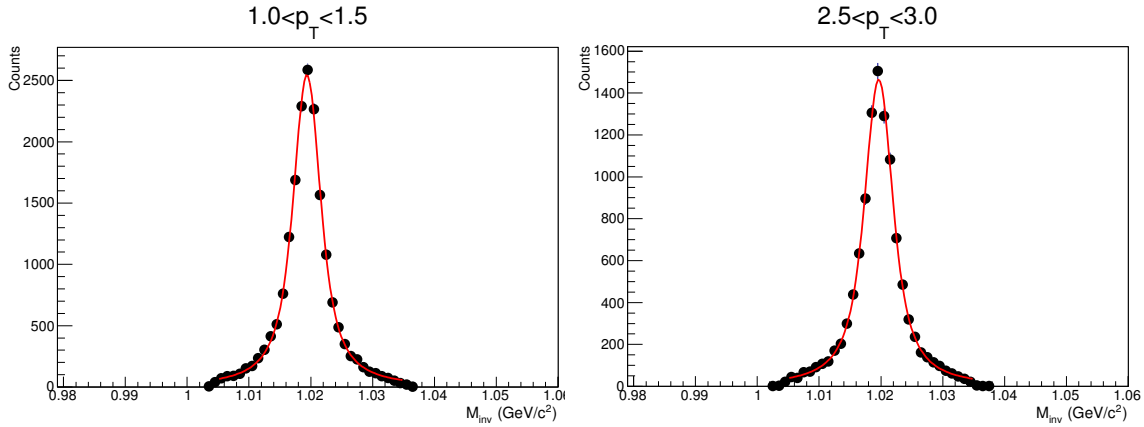

Figure 2: Reconstructed histogram with a Voigtian0 fit, where σ_{voi} is obtained. The left plot is shown in the transverse momentum $1.0 < p_{\mathrm{T}} < 1.5$ and the right plot in $2.5 < p_{\mathrm{T}} < 3.0$, both in the multiplicity bin $0 - 100\%$

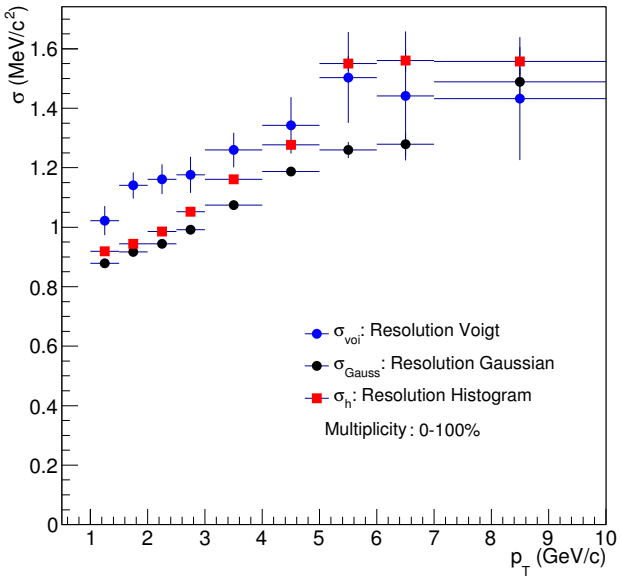

Figure 3: Three calculations of the resolution are presented, σ_{Gauss}, σ_h, σ_{voi} in the 0-100% multiplicity bin.